VLTI Community Days, January 15-16, 2014, Grenoble, France

AMBER

VLTI, general user, 3T, K,H,J spectro-interferometric instrument

Romain Petrov

Laboratoire LAGRANGE,

OCA – UNS - CNRS

And the AMBER Consortium

Nice – Grenoble – Bonn – Firenze – ESO

amber.obs.ujf-grenoble.fr

Foreword

Rank A articles tagged by instrument

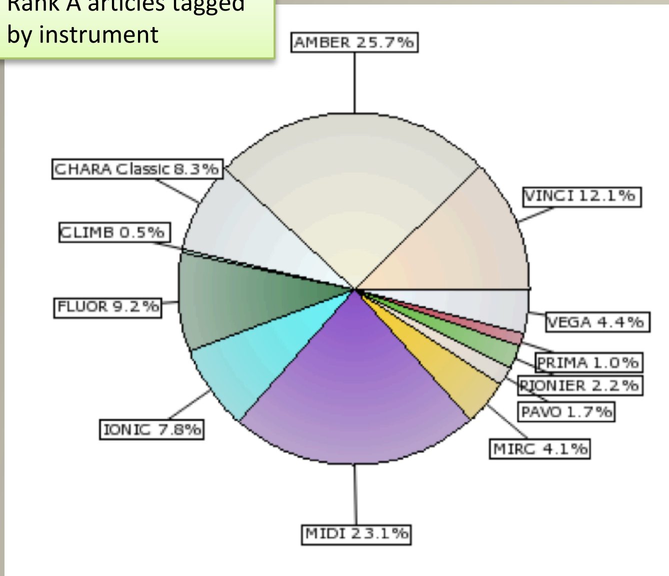

Rank A articles tagged by AMBER (106)

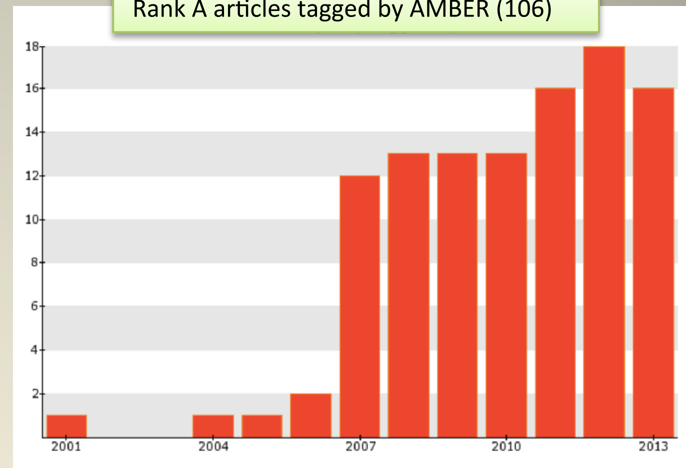

AMBER is the most productive Optical Interferometric Instrument ever, in number of science papers

AMBER is still at its science publication peak

In December 2013, 96 rank papers have been accepted on 21 science topics. Reviewing all results or even topics in 20 minutes is impossible

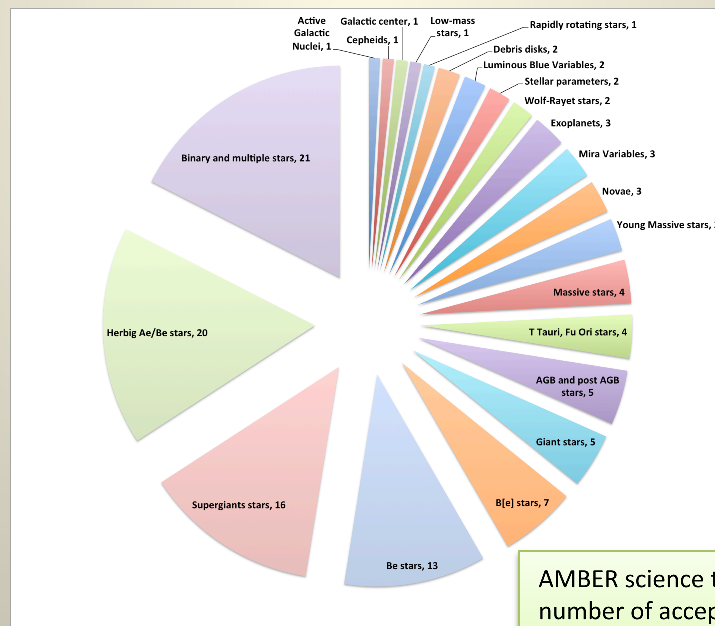

AMBER science topics by number of accepted rank A articles (12/2013)

From JMMC-OLBIN publications Database, January 2014

AMBER, near IR VLTI focal instrument

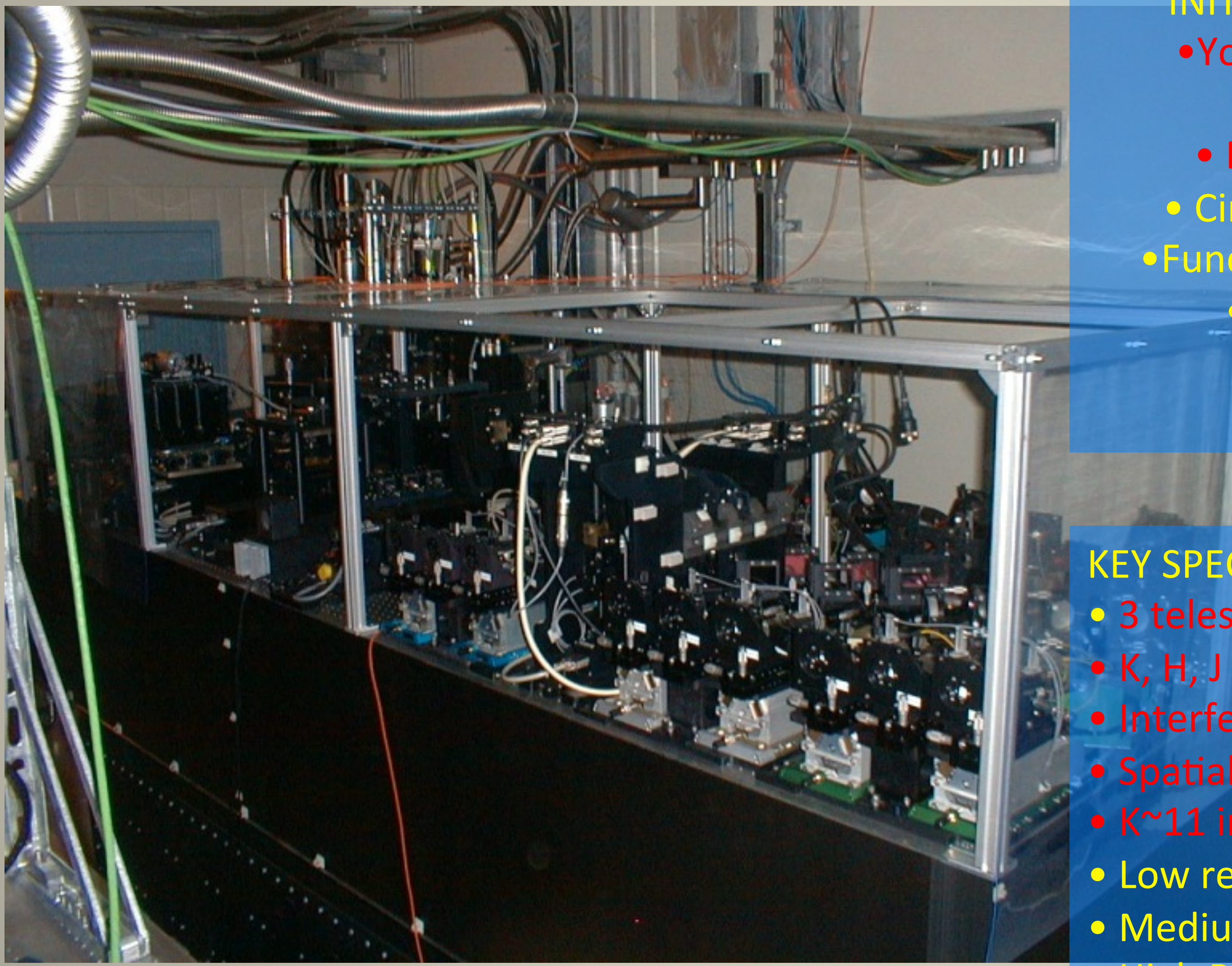

INITIAL SCIENCE GOALS

- Young Stellar Objects
- AGN
- Extra Solar Planets
- Circumstellar material
- Fundamental parameters
- Distance scales
- Stellar activity
- Asteroids

KEY SPECIFICATIONS

- 3 telescopes
- K, H, J bands
- Interferometry + Spectroscopy
- Spatial filtering
- K~11 in low resolution
- Low resolution: 35
- Medium resolution: 1500
- High Resolution: 12 000

Plan

- Goals and results
  - Extrasolar planets
  - Young stars
  - Be and B[e]
  - Novae
  - LBV
  - Super giant stars
  - AGNs
  - …

- Measures and methods
  - Very high accuracy
  - All, including imaging
  - Spectro-interferometry
  - Spectro-interferometry
  - Spectro-interferometry at HSR
  - Faint targets

AMBER Key Dates

- 1997: proposal to ESO of a 3T near-IR & visible instrument
- 1999: AMBER CDR
- 2000: AMBER PDR: concept frozen
- 2001: AMBER FDR
- 2003: AMBER PAE
- 2004: AIV Paranal
- 2005: First Science with UTs
- 2007: A&A special issue with first results
- 2009: Correction of beatings in polarization filters: full capacity in MR/HR
- 2010: PAC
- 2011: 2DFT processing: K>10 in MR (K>11 in LR): achieve intended sensitivity
- 2013: Spectrograph maintenance

AMBER data and measures

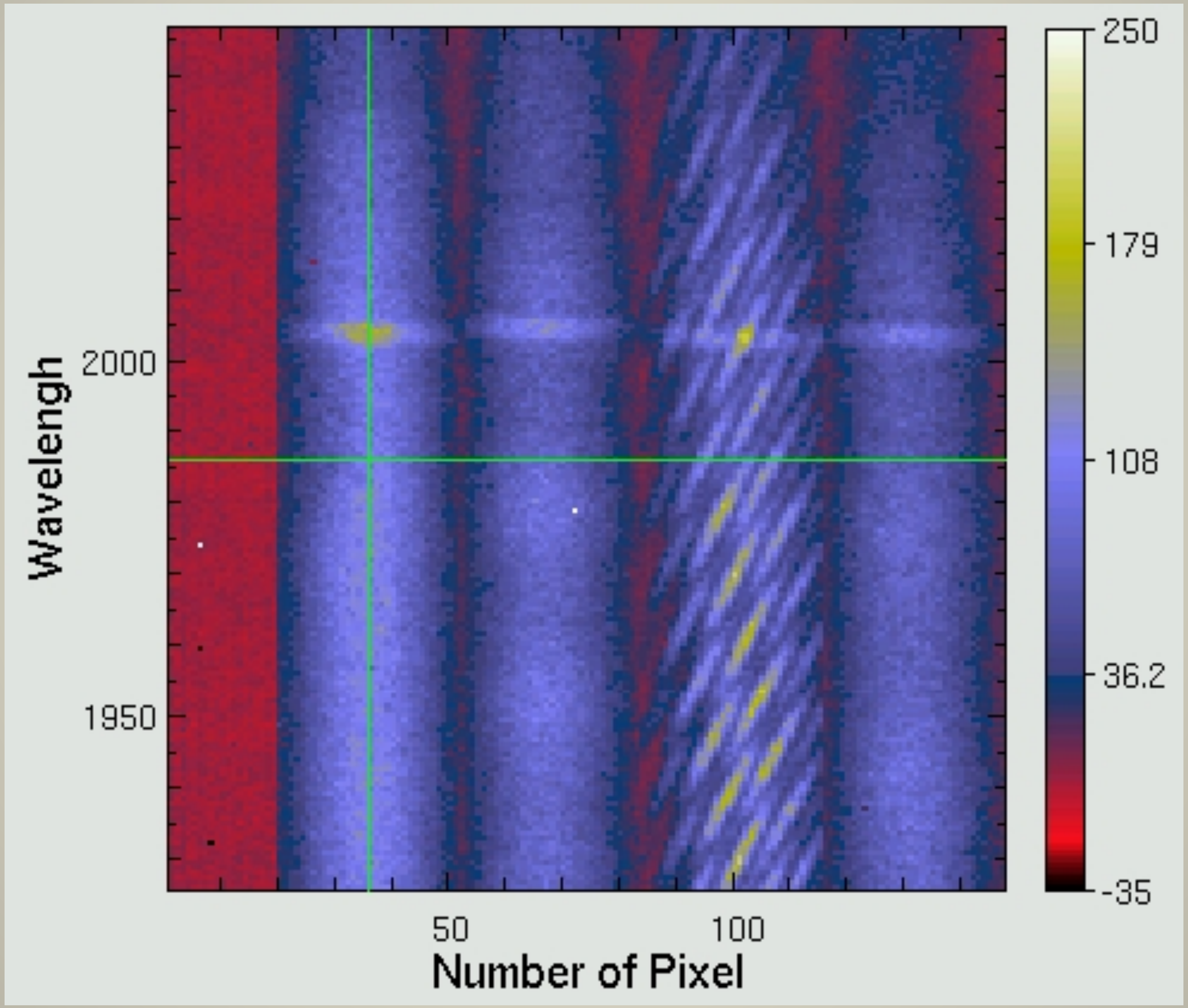

AMBER data and measures

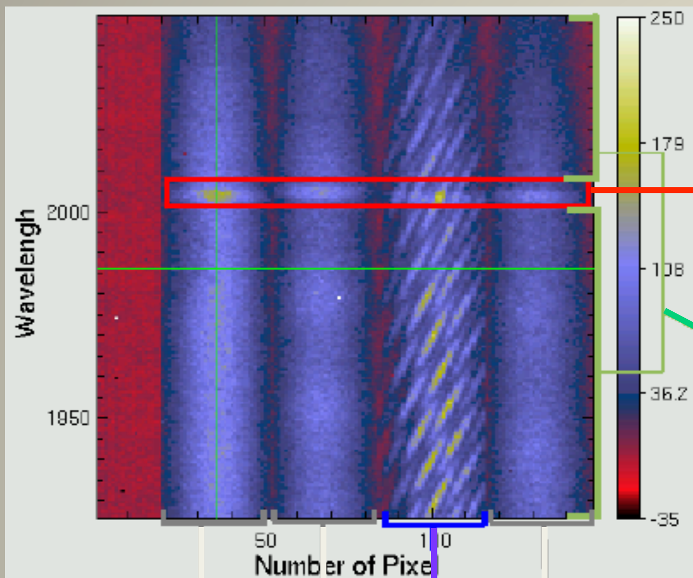

Work channel at λ: $C_i(\lambda)$

Reference channel averaged over Δλ: $C_{iref}=\sum_{\Delta\lambda} C_i(\lambda)$

Photometric beams

Interferometric beam

Complex Visibility per frame: $C_i(\lambda)$
(corrected for the achromatic piston)

AMBER data and measures

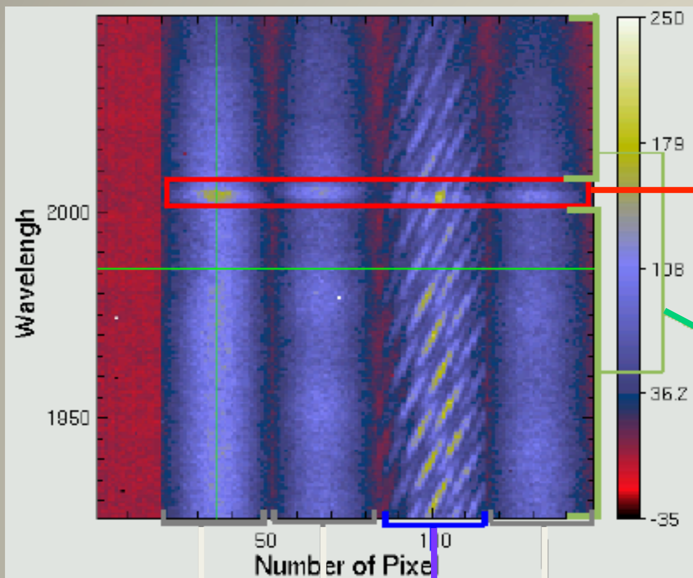

Work channel at λ: $C_i(\lambda)$

Reference channel averaged over Δλ: $C_{iref}=\sum_{\Delta\lambda} C_i(\lambda)$

Photometric beams

Interferometric beam

Complex Visibility per frame: $C_i(\lambda)$
(corrected for the achromatic piston)

- Spectrum $S(\lambda)$
- Visibility = $V_i(\lambda) = \sqrt{<|C_i(\lambda)|^2>_{frames}}$
- Differential Visibility: $V_{id}(\lambda) = \sqrt{Re[<C_i(\lambda)C_{iref}^*>_{frames}]}$
- Differential Phase: $\Phi_{id}(\lambda) = \tan^{-1}(<C_i(\lambda)C_{iref}^*>_{frames})$
- Closure phase: $\Psi_{123}(\lambda) = \tan^{-1}[<C_1(\lambda)\, C_2(\lambda)\, C_3^*(\lambda)>_{frames}]$

Petrov et al., A&A 2007

Faint companions: Piston noise error

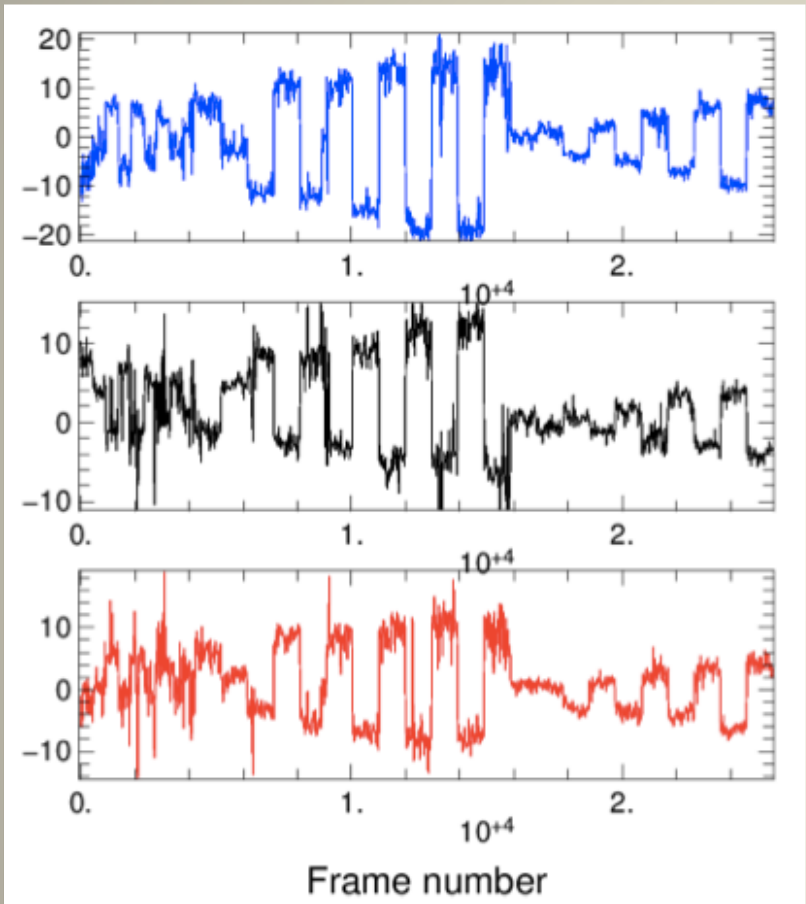

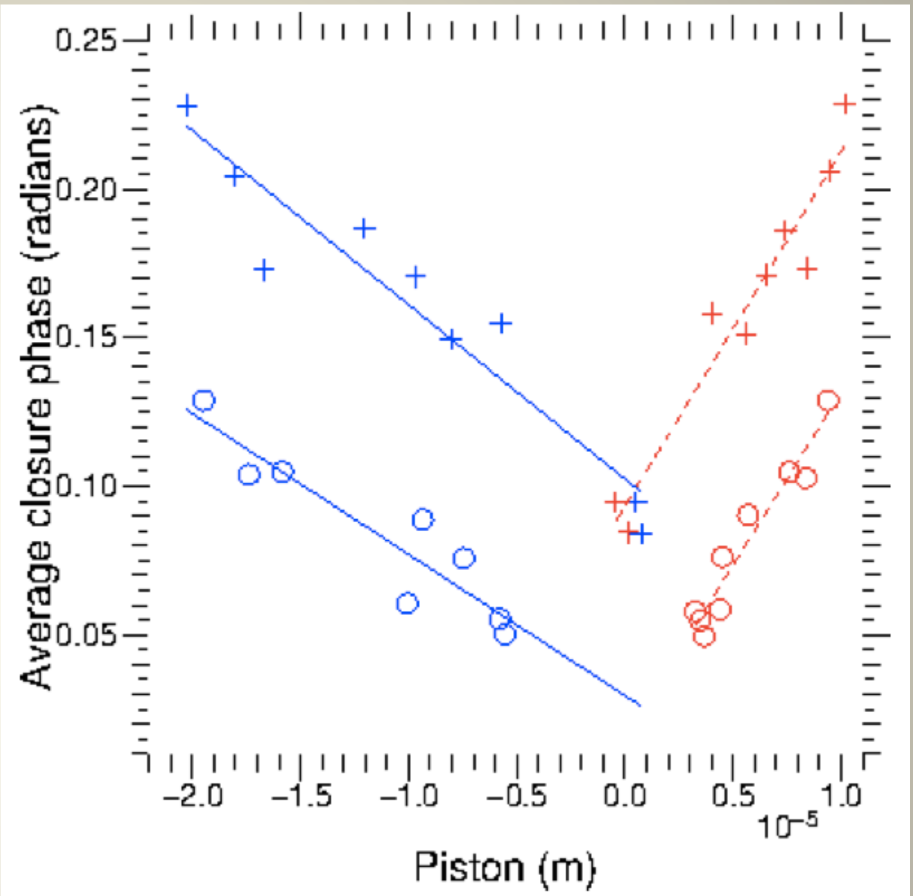

Vannier et al, SPIE 2012

- The closure phase errors are dominated by piston noise, most likely due to "Group Delay cross talk".

Faint companions: Closure phase errors

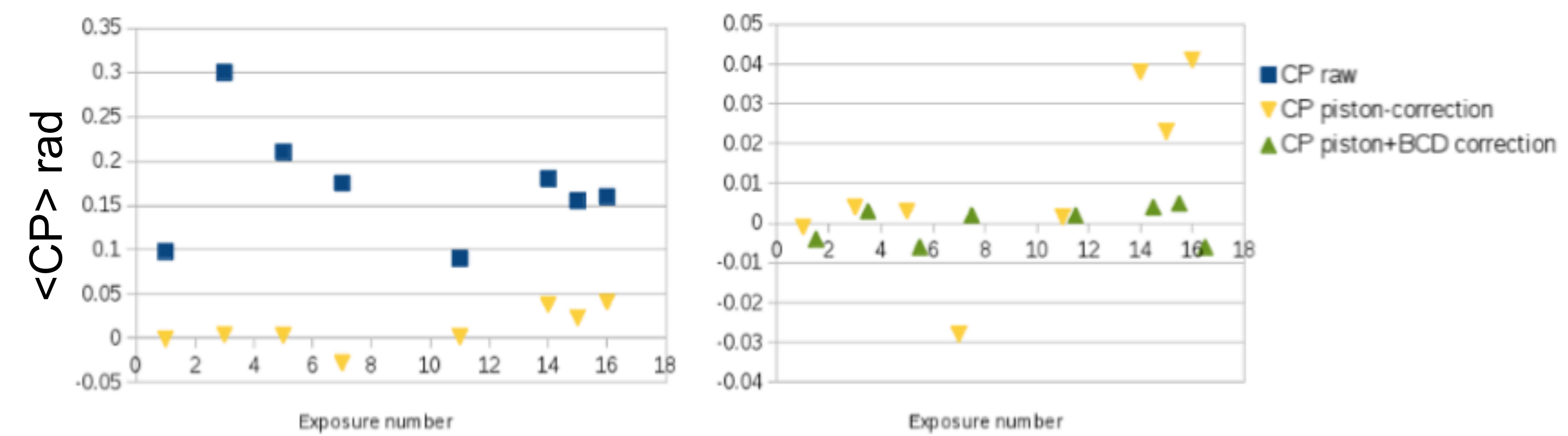

Figure 4. *Left: Examples of values of uncalibrated average CP observed in "standard mode" (squares), with a mean value* $< CP >= 2.8$ *deg (0.14 rad) and a standard deviation* $\sigma \approx 2.8$ *deg (0.05 rad); and after a correction of the piston linear dependency (yellow triangles) using a linear fit as shown in Fig.3, where* $< CP > \approx 0.34$ *deg (6 mrad) and* $\sigma \approx 0.6$ *deg (0.01 rad). Right: Values of average CP after piston effect correction (yellow triangles, same as in left-side figure, different scale), and after and additional internal calibration using the BCD (green upward triangles). With the overall correction,* $< CP >= 3.7$ *deg (6.5 mrad) and* $\sigma = 0.12$ *deg (2.2 mrad).*

Vannier et al, SPIE 2012

- The closure phase errors are dominated by piston noise, most likely due to "Group Delay cross talk"
- Thus they are sensitive to chromatic piston (i.e. dispersion) errors
- There are other error sources (detector changes) which can improved by fast calibration with a Beam Commutation
- Can be corrected if there is a sample of pistons (including with FT)
- MATISSE has modulations that reduce the cross-talks below 10^{-5} and BCDs

Faint companions and High Accuracy on closure and differential phase

Best differential phase	**4 milliradians**
Best closure phase	**2 milliradians**
Dynamics for faint companion	**~1/1000**

VLT-TRE-AMB-15830-7021

Figures 5.3c and 5.3d : correction of the differential phase with a calibrator.

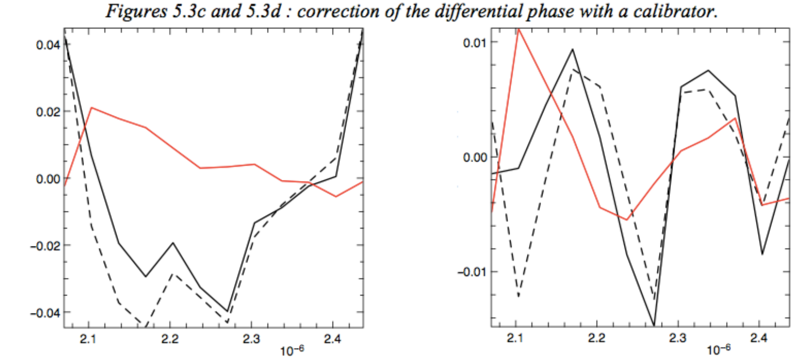

Phase in radians as a function of wavelength in microns. Full dark line=source ; dashed dark line=calibrator ; red line = calibrated phase = calibration error in this case with two calibrators.

Figure 5.3c: STD observation calibration error after chromatic OPD fit:

- PTV=0.025 radians=1.5°
- RMS=0.009 radians=0.5°

Figure 5.3d: BCD observation calibration error after chromatic OPD fit:

- PTV=0.017 radians=1°
- RMS=0.004 radians=0.2°

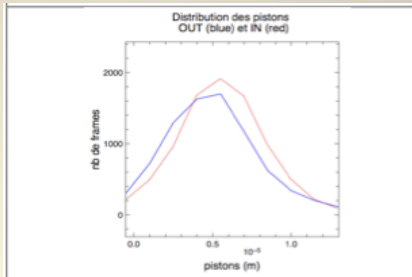

Histogram of measured pistons on calibrator 2. The average piston with BCD_out is x=4.9 µm. The average -piston with BCD_in is x=5.5 µm. The average piston for (out-in)/2 is x=5.2 µm. Note the change in pistons, including the piston difference between bcd_out and bcd_in.

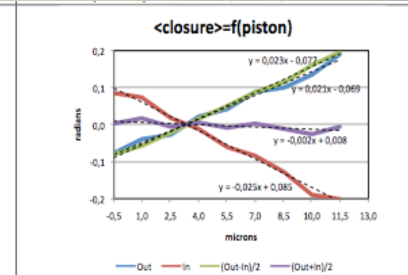

Fit of closure phase average as a function of the piston class x (i.e. piston in [x,x+1.5]). x=<p>-0.75. Calibrator 2. Note that the slopes and offsets of the fits are different from calibrator 1.

- BCD_out: x=4.9, $<\Psi_{MO}>$= 34 mrad
- (out-in)/2: x=5.2, $<\Psi_{MU}>$= 43 mrad

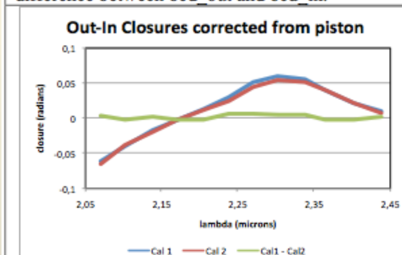

BCD Closure phase corrected from average pistons.

- $<\Psi_{MO}> = 2.6$ mrad
- $\sigma_{\Psi MO} = 2.0$ mrad

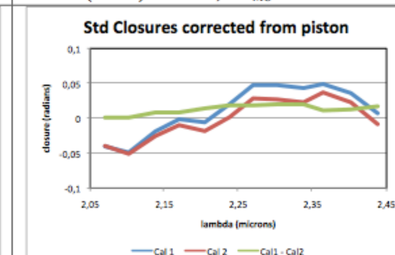

Standard Closure phase corrected from average pistons.

- $<\Psi_{MO}> = 13$ mrad
- $\sigma_{\Psi MO} = 6.6$ mrad

Not enough for Hot Jupiters
Possible program for faint companions (1/1000) in the range 0.25 to λ/B

MWC 297

(first AMBER science result,
second most cited AMBER science paper)

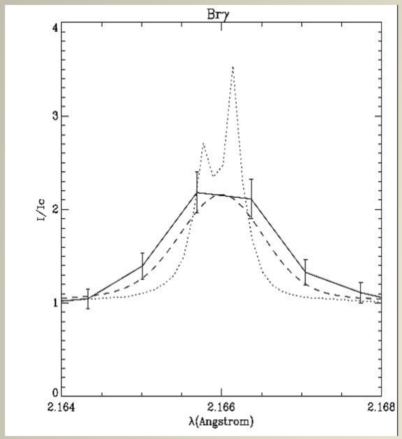

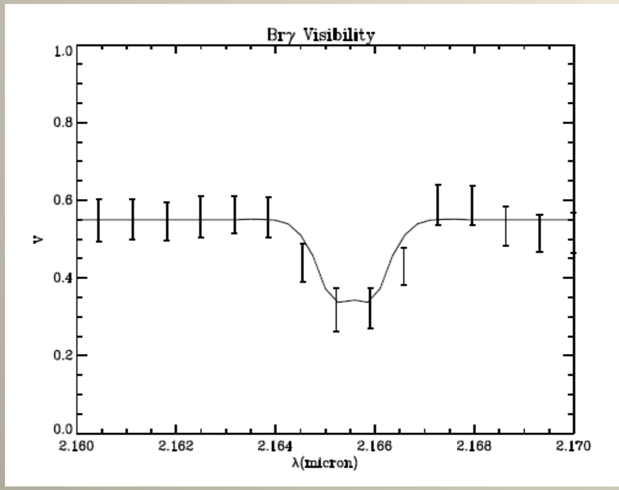

- ISAAC Br_γ profile: Br_γ region is 140 R_*
  - Keplerian rotation
  - Peaks separation= $v_0 \sin i \,(r/R_*)^{-x}$

- AMBER differential visibility: Br_γ region is 43 R_*
  - Good fit if the optically thick disk masks partially the wind

Malbet et al., A&A 2007

MWC 297

(first AMBER science result,
second most cited AMBER science paper)

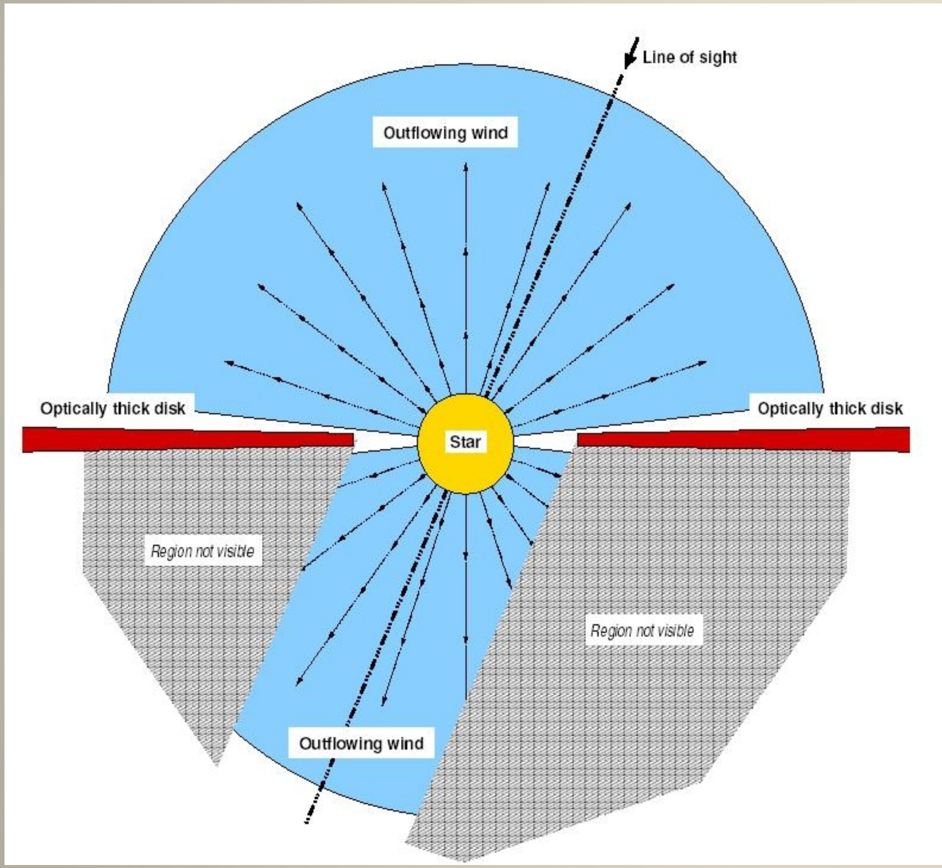

- ISAAC Br_γ profile: Br_γ region is 140 R_*
  - Keplerian rotation
  - Peaks separation= $v_0 \sin i \, (r/R_*)^{-x}$

- AMBER differential visibility: Br_γ region is 43 R_*
  - Good fit if the optically thick disk masks partially the wind

Malbet et al., A&A 2007

MWC 297

(first AMBER science result,
second most cited AMBER science paper)

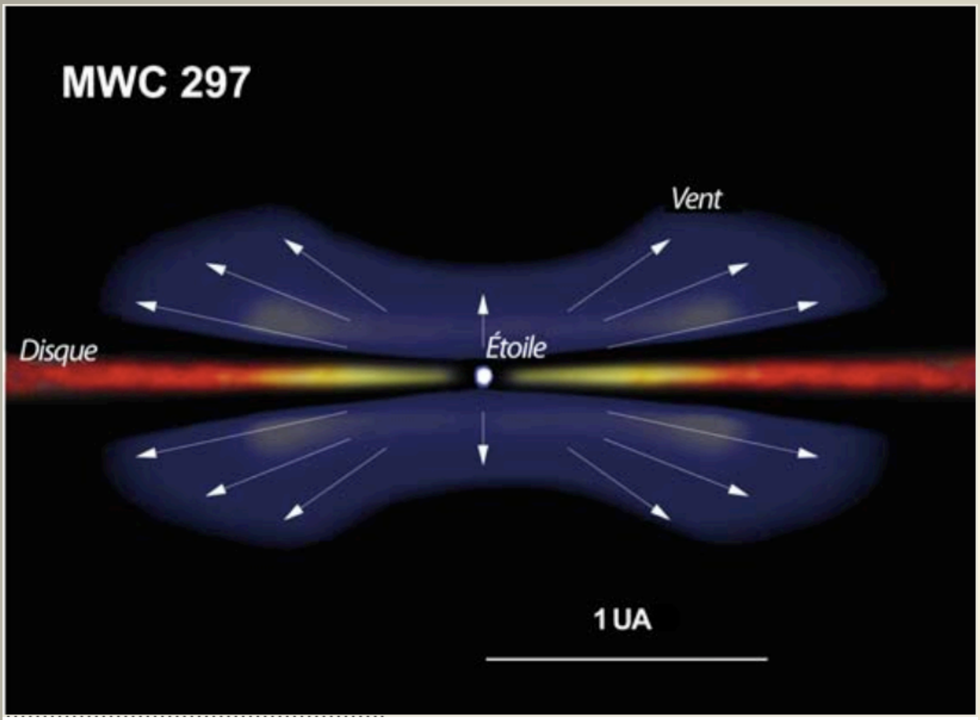

Photospheric density	$1 \pm 0.5 \times 10^{12}$ cm^{-3}
Equatorial rotational velocity	400 ± 50 km s^{-1}
Polar terminal velocity	600 ± 50 km s^{-1}
Terminal velocity above disk	70 ± 20 km s^{-1}
Polar mass flux	$3.2 \pm 0.2 \times 10^{-9}$ $M_\odot$ yr^{-1}
C_1	0.25 ± 0.05
m_1	30 ± 10
m_2	10 ± 2
Inclination angle (i)	$25 \pm 5°$

- ISAAC Br_γ profile: Br_γ region is 140 R_*
  - Keplerian rotation
  - Peaks separation= $v_0 \sin i \, (r/R_*)^{-x}$

- AMBER differential visibility: Br_γ region is 43 R_*
  - Good fit if the optically thick disk masks partially the wind

Malbet et al., A&A 2007

MWC 297 at resolution 12000

- Very compact continuum disk (0.5 AU, while sublimation radius is 3 AU)
- Wind produced in inner part of the disk
- Very open wind distribution (80°) because of strong radiation pressure of massive star
- Almost pole on object
- Accurate model of kinematics

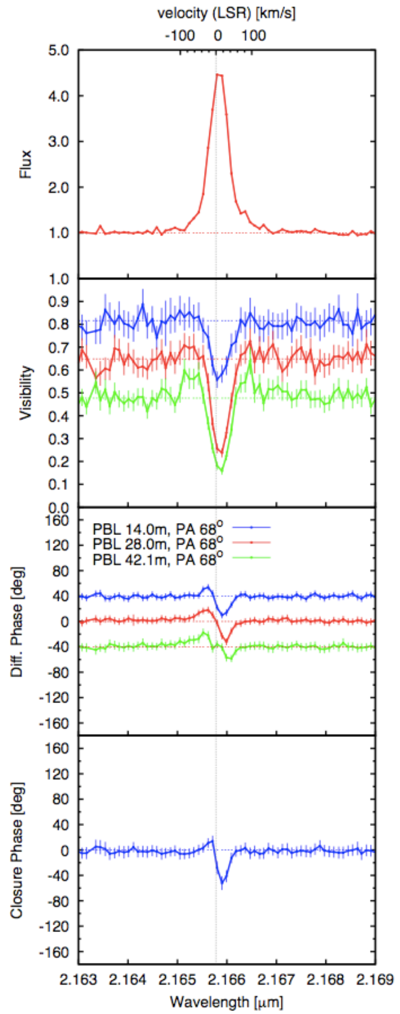

Fig. 1. AMBER observations of MWC 297 with spectral resolution of 12 000: (from top to bottom) wavelength dependence of flux, visibilities, wavelength-differential phases (for better visibility, the differential phases of the shortest and longest baselines are shifted by +40 and −40°, respectively), and closure phase observed at projected baselines of 14.0, 28.0, and 42.1 m along the position angle (PA) of 68.0° on the sky. The wavelength scale at the bottom is the directly observed one, i.e. without heliocentric or LSR correction (see text). However, the radial velocity scale at the top, gives spectrum, visibilities, and phases as a function of the Brγ Doppler shift in the Local Standard of Rest (LSR) frame. The dashed vertical line indicates the centroid Brγ vacuum wavelength (2.1661 μm) in the LSR frame.

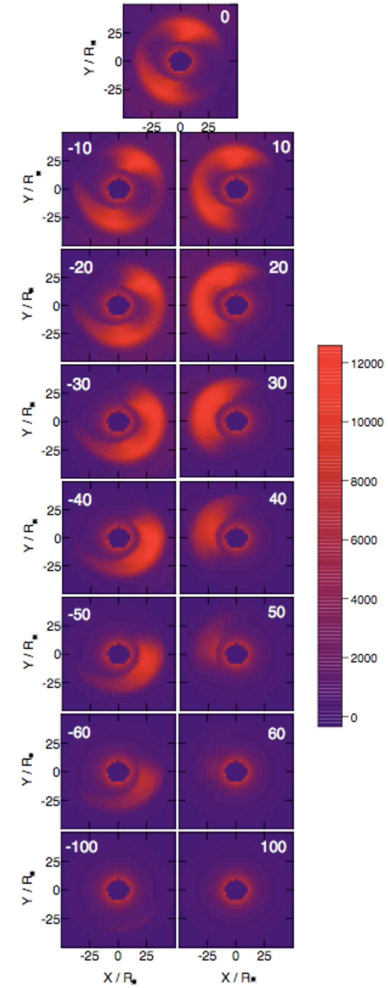

Fig. 5. Intensity distributions of our best-fit disk-wind model 5 (i.e., intensity distribution of the continuum disk plus the disk wind; the central star is not shown; see Tables 3 and A.1) at the center of the Brγ line (v = 0 km s^{-1}) and at 14 other velocities (the labels give the velocity in km s^{-1}). For the calculation of the model images in this figure, a clockwise motion of the disk wind was assumed. Therefore, in the blue-shifted images (left panels), mainly the disk regions on the right hand side of the star are bright. The radius of the inner edge of the disk wind ejection region (i.e., radius of the inner hole) is ω_1 = 17.5 R_* (~0.3 AU). The inclination angle (angle between the polar axis and the viewing direction) of the model is i = 20° (i.e., almost pole-on). The colors represent the intensity in erg ster^{-1} s^{-1} Å^{-1} cm^{-2}. In these images, AMBER's spectral resolution of 12 000 was modeled, as described in Sect. A.3

Weigelt et al., A&A 2011

MWC 297 at resolution 12000

Table 3. Range of parameter variations for our continuum-disk plus disk-wind model calculations

Parameters	Range	Model 5
Disk:		
R_{in}	0.25–3 AU (8.8–105 R_*)	0.3 AU (10.5 R_*)
R_{out}	1–5 AU (35–175 R_*)	3 AU (105 R_*)
R_s	0.85–1.25 AU (30–44 R_*)	0.9 AU (31.5 R_*)
α_1	-0.4– -0.75	-0.5
α_2	-0.34– -0.4	-0.33
T_{in}	1400–2000 K	1800 K
Disk wind:		
ω_1	0.1–3 AU (3.5–105 R_*)	0.5 AU (17.5 R_*)
ω_N	0.5–5.7 AU (17.5–200 R_*)	1 AU (35 R_*)
γ	-1–5	2
f	0.5–3	0.5–3
β	0.3–2	1
θ_1	10°–80°	80°
$\dot{M}_w$	10^{-9}–$10^{-6} M_\odot yr^{-1}$	$10^{-7} M_\odot$ yr^{-1}

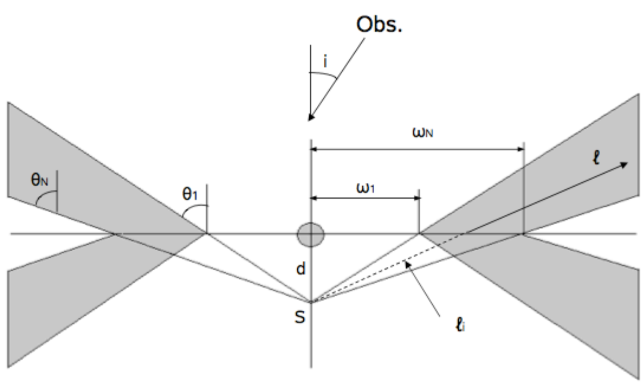

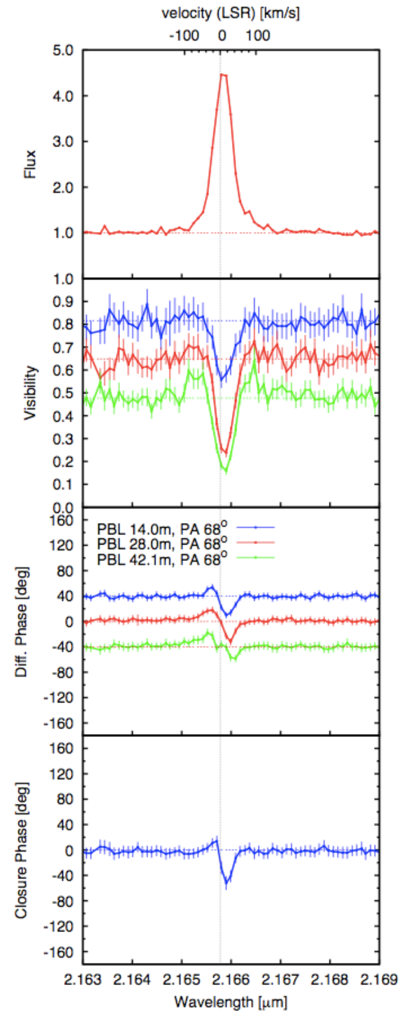

Fig. 1. AMBER observations of MWC 297 with spectral resolution of 12 000: (from top to bottom) wavelength dependence of flux, visibilities, wavelength-differential phases (for better visibility, the differential phases of the shortest and longest baselines are shifted by +40 and −40°, respectively), and closure phase observed at projected baselines of 14.0, 28.0, and 42.1 m along the position angle (PA) of 68.0° on the sky. The wavelength scale at the bottom is the directly observed one, i.e. without heliocentric or LSR correction (see text). However, the radial velocity scale at the top, gives spectrum, visibilities, and phases as a function of the Brγ Doppler shift in the Local Standard of Rest (LSR) frame. The dashed vertical line indicates the centroid Brγ vacuum wavelength (2.1661 μm) in the LSR frame.

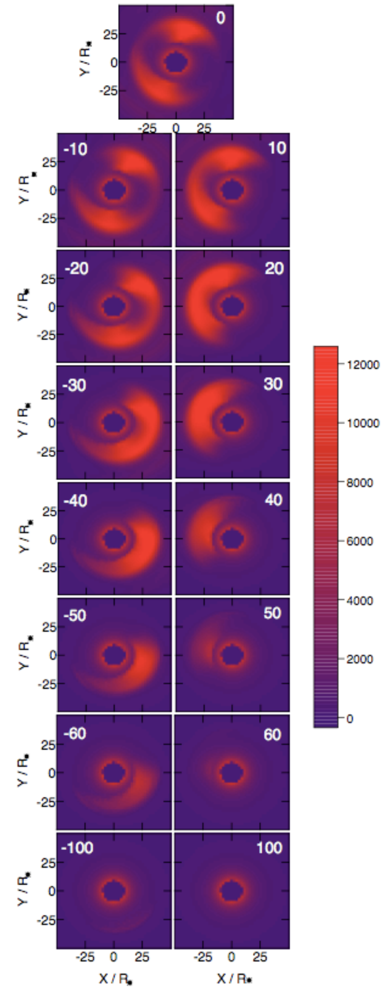

Fig. 5. Intensity distributions of our best-fit disk-wind model 5 (i.e., intensity distribution of the continuum disk plus the disk wind; the central star is not shown; see Tables 3 and A.1) at the center of the Brγ line (v = 0 km s^{-1}) and at 14 other velocities (the labels give the velocity in km s^{-1}). For the calculation of the model images in this figure, a clockwise motion of the disk wind was assumed. Therefore, in the blue-shifted images (left panels), mainly the disk regions on the right hand side of the star are bright. The radius of the inner edge of the disk wind ejection region (i.e., radius of the inner hole) is ω_1 = 17.5 R_* (∼0.3 AU). The inclination angle (angle between the polar axis and the viewing direction) of the model is i = 20° (i.e., almost pole-on). The colors represent the intensity in erg ster^{-1} s^{-1} Å^{-1} cm^{-2}. In these images, AMBER's spectral resolution of 12 000 was modeled, as described in Sect. A.3

Weigelt et al., A&A 2011

“Non spectroscopic” results: HR5999 and the inner rim of the dust disk

- Massive young star
- Good u-v coverage (many observations)
- Best image of inner rim of dust disk with central hole

- Historical AMBER Image

- PIONIER does better

  See Myriam Benisty’s presentation

- AMBER is for kinematics

M. Benisty et al.: HR 5999 inner disk

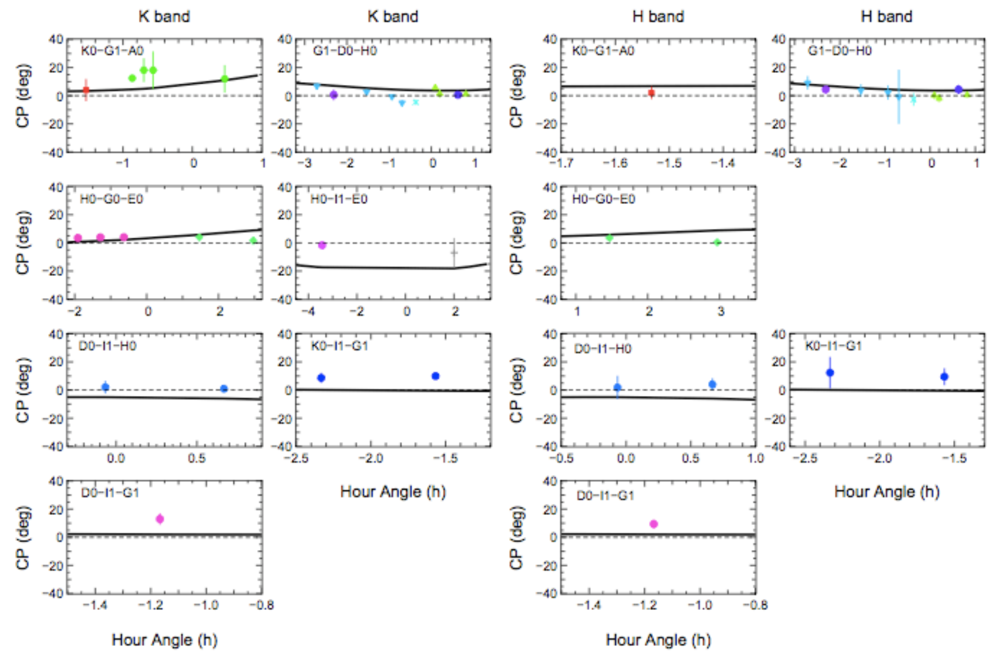

Fig. 4. The black curves give the predictions of the two-component disk model for the broad-band closure phases in the *K*-band (*left columns*) and in the *H*-band (*right columns*). Each panel corresponds to a different telescope configuration, and the color code is the one of Figs. A.1 and A.3.

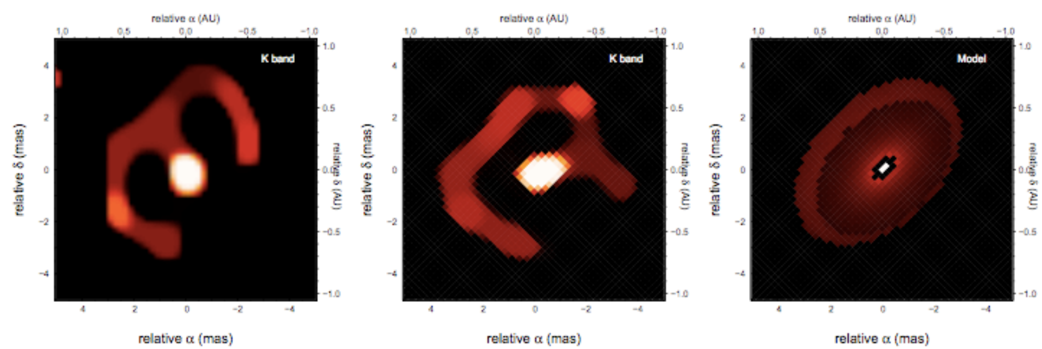

Fig. 5. The *K*-band image is shown, as reconstructed from the AMBER measurements (*left*), and as reconstructed from the simulated data from the model (*middle*). The latter is shown in *the right panel*. The images are shown on a 10 mas × 10 mas scale.

Differential visibility and phase in line
The classical Be star α Arae
(most cited AMBER science paper)

The classical Be star: B3Ve, T_{eff}=18000K, M_*= 9.6$M_\odot$, R_*= 4.8$R_\odot$, L_*= 5.8 10^3 $L_\odot$, i=45°, v_e sin*i*=300 km/s, $v_{e\infty}$=179 km/s, $v_{p\infty}$=2000 km/s

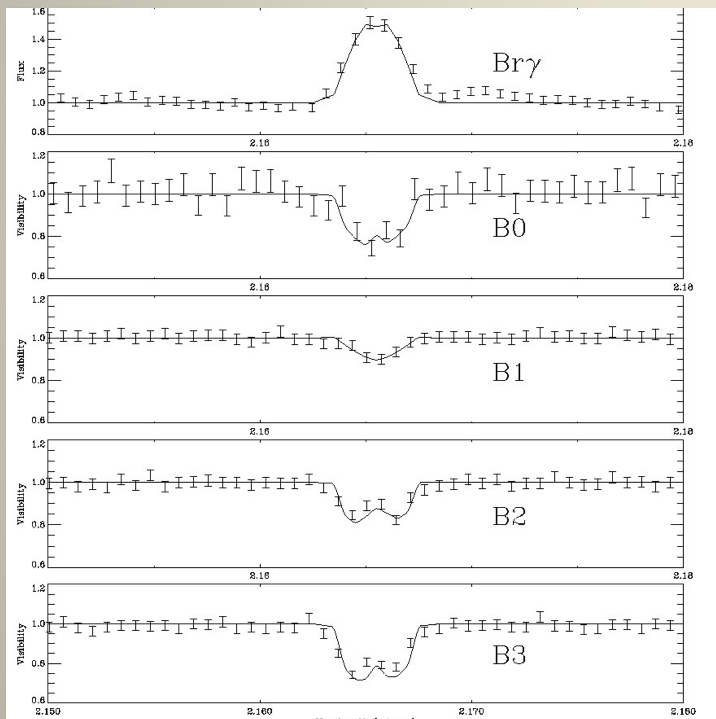

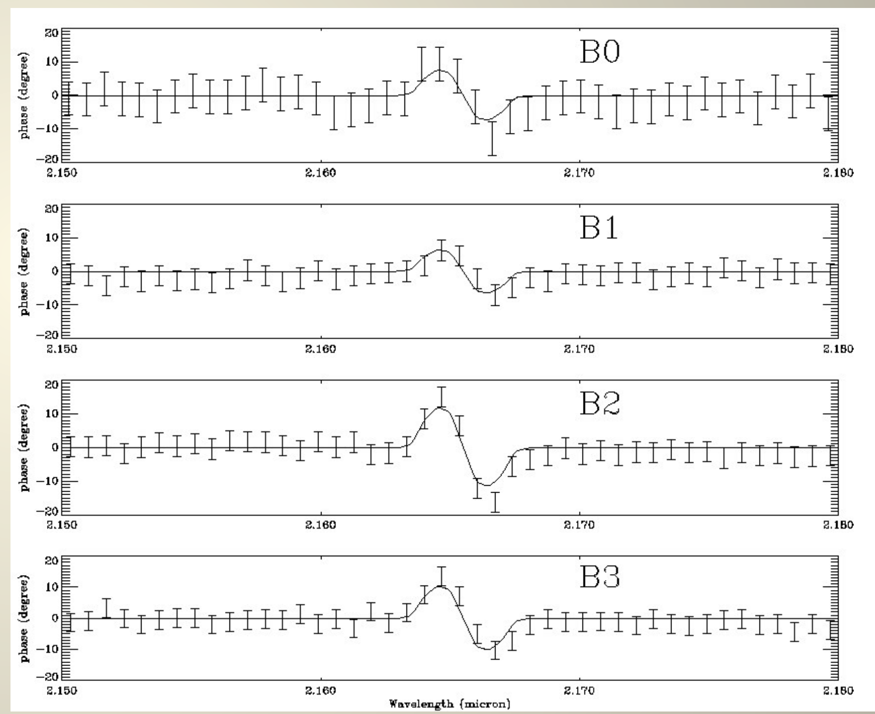

Line profile and Differential visibility

Differential phase

Stee et al., A&A 2007

Differential visibility and phase in line
Keplerian rotation in α Arae disk
(a question since 1866…)

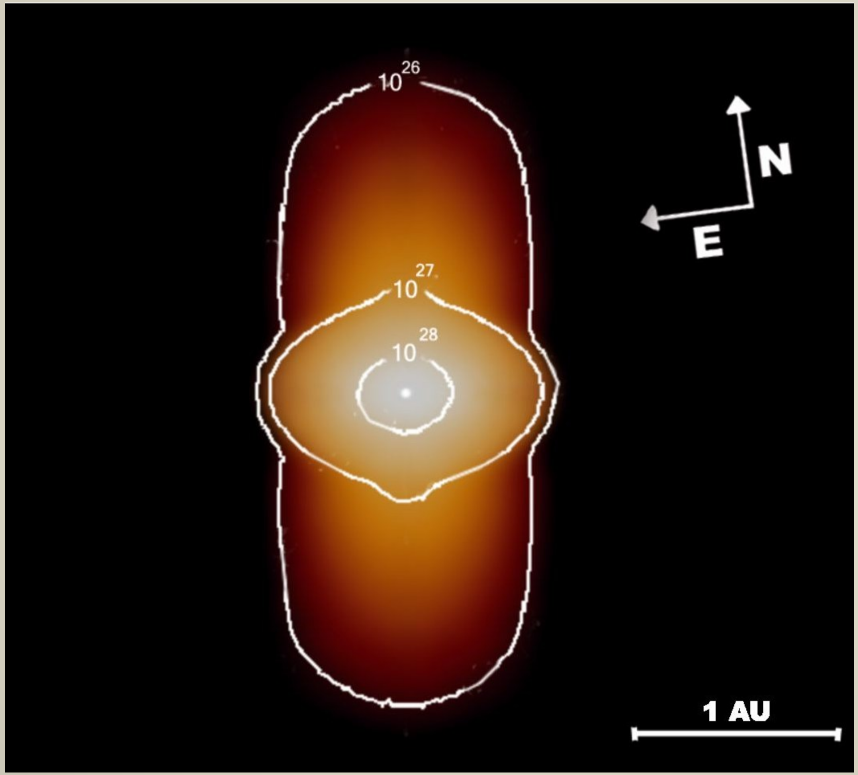

Brightness map computed by the SIMECA code (cont @ 2μm)

Stee et al., A&A 2007

Differential visibility and phase in line
Keplerian rotation in α Arae disk
(a question since 1866…)

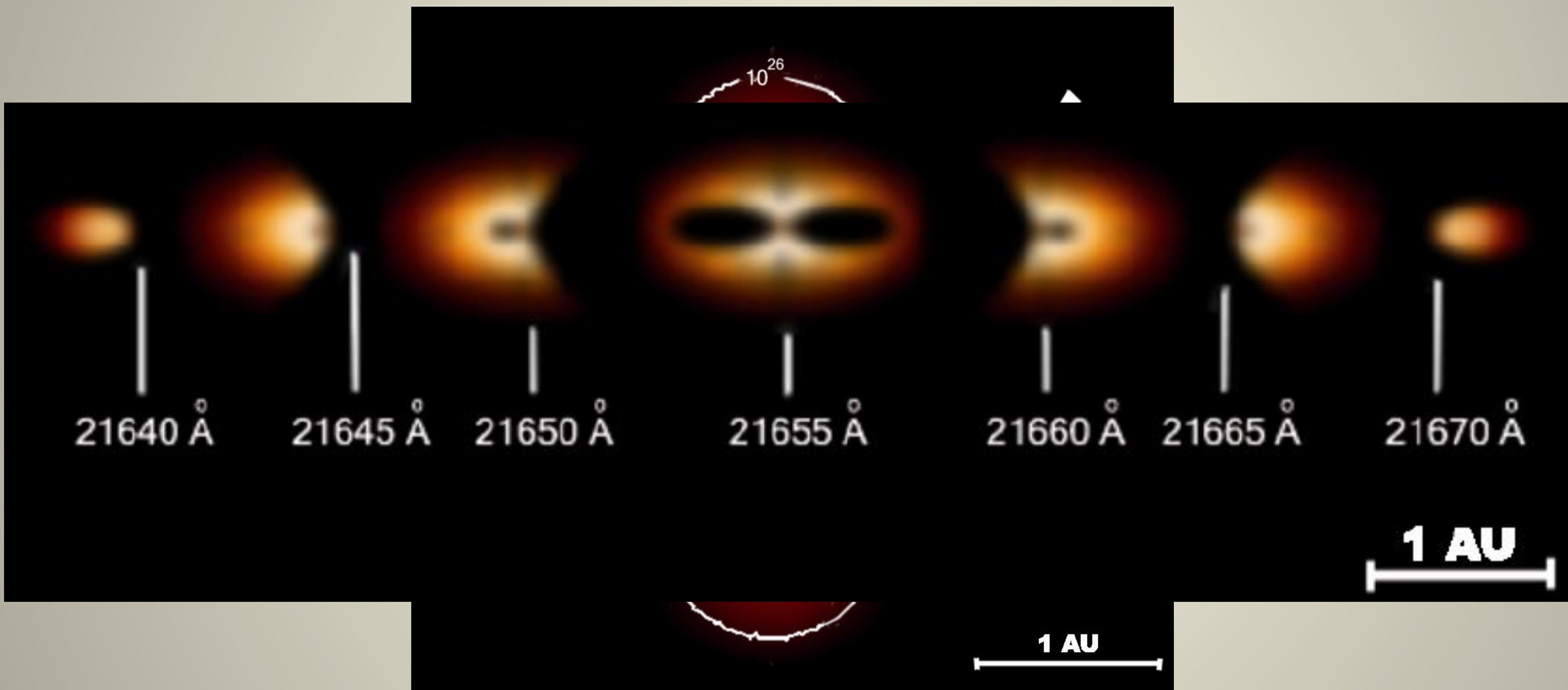

Envelope images in equal velocity bins through Brγ

Stee et al., A&A 2007

Differential visibility and phase in line
Keplerian rotation in α Arae disk
(a question since 1866…)

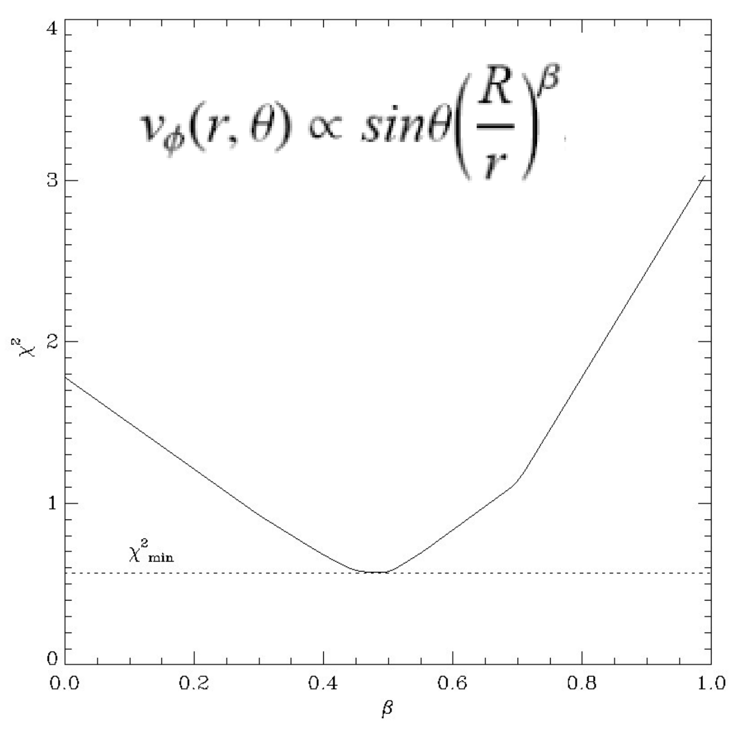

χ^2 as a function of the velocity law parameter β

- β = 0 ➔ constant rotation
- β = 0.5 ➔ Keplerian rotation
- β = 1 ➔ constant angular momentum

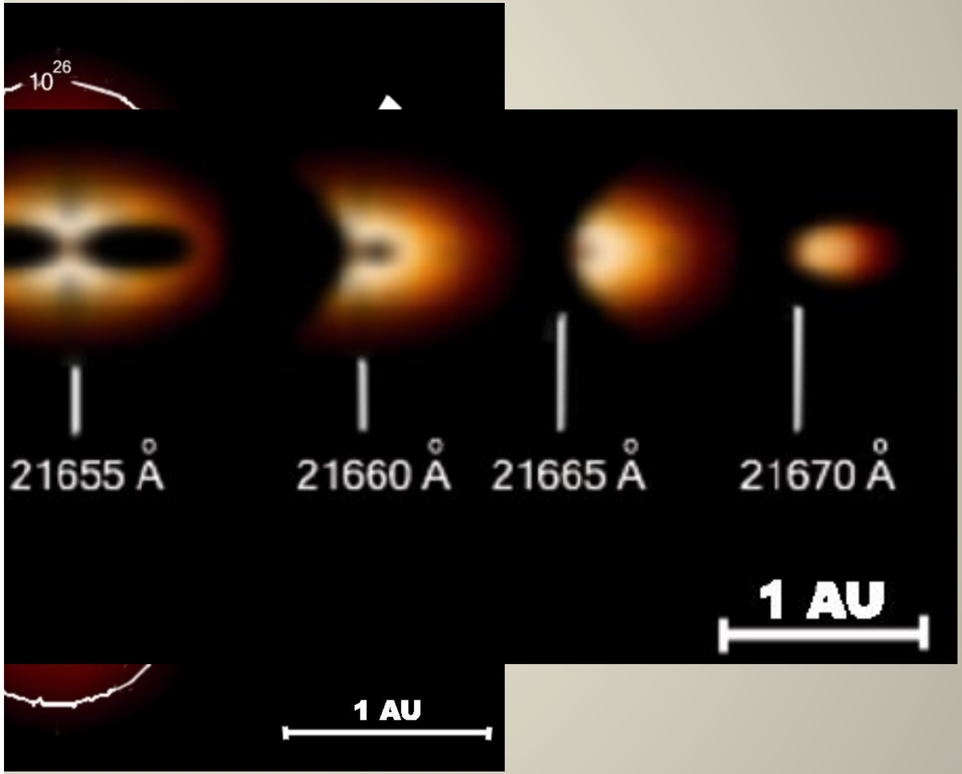

Stee et al., A&A 2007

Non axisymmetric envelope of κ Cma and many other Be and B[e]results

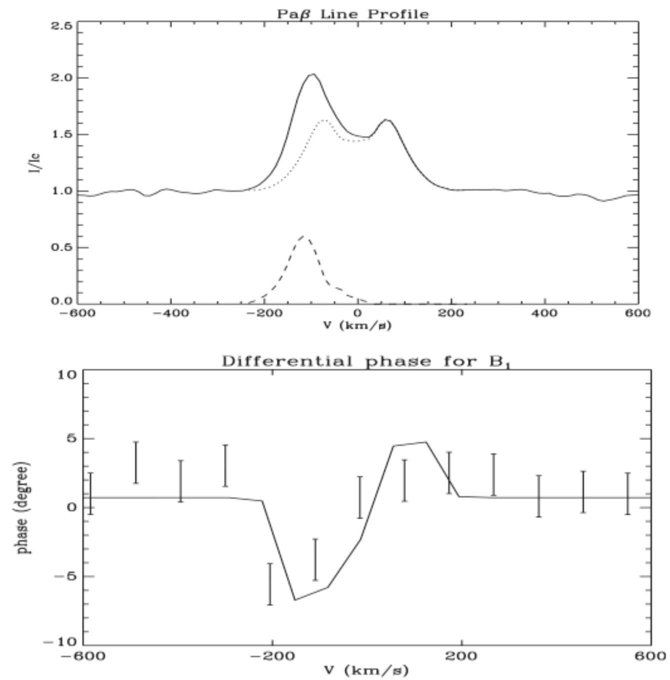

Fig. 5. *Upper picture*: κ CMa Paβ line profile observed in December 2005 at the Observatorio do Picos dos Dias, Brazil (solid line). Estimated symmetric part of the Paβ profile (dotted line) using an axi-symmetric model. The asymmetric residue corresponds to the emission of "one-armed" over-density (dashed line). *Bottom picture*: differential phase variation measured along the B_1 baseline (dots with errors bars) and theoretical phase from the SIMECA code.

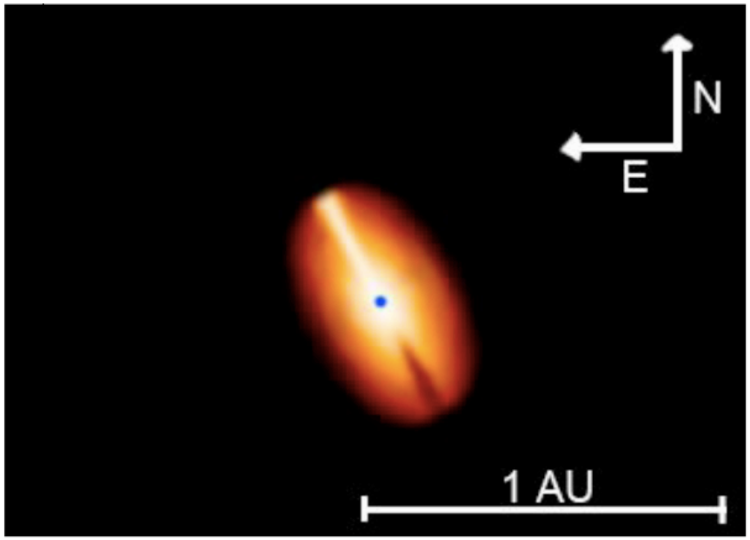

Fig. 6. Intensity map in the continuum at 2.15 μm obtained with SIMECA for our best model parameters. The inclination angle is 60°, the central black dot represents the κ CMa photosphere (0.25 mas); the bright part in the equatorial disk is produced by the over-density which is oriented along the B_1 baseline. This over-density is also responsible for a 30% emission excess in the asymmetric *V* part of the Brγ line.

Meilland et al., A&A 2007

Non axisymmetric envelope of ζ Tau

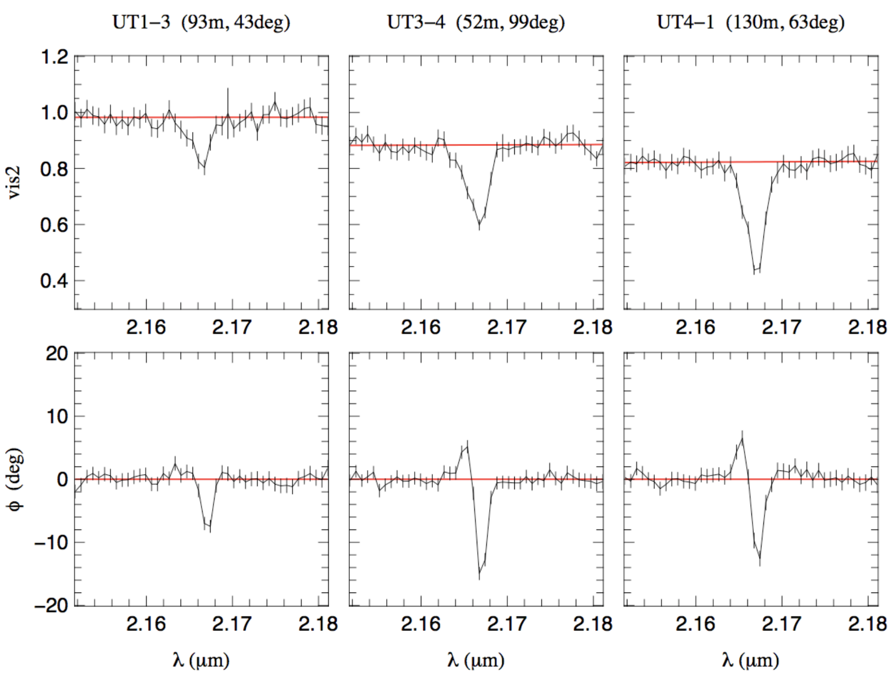

Fig. 11. AMBER visibilities and phases around 2.18 μm normalized to the model of Gies et al. (2007).

Stefl et al., A&A 2009

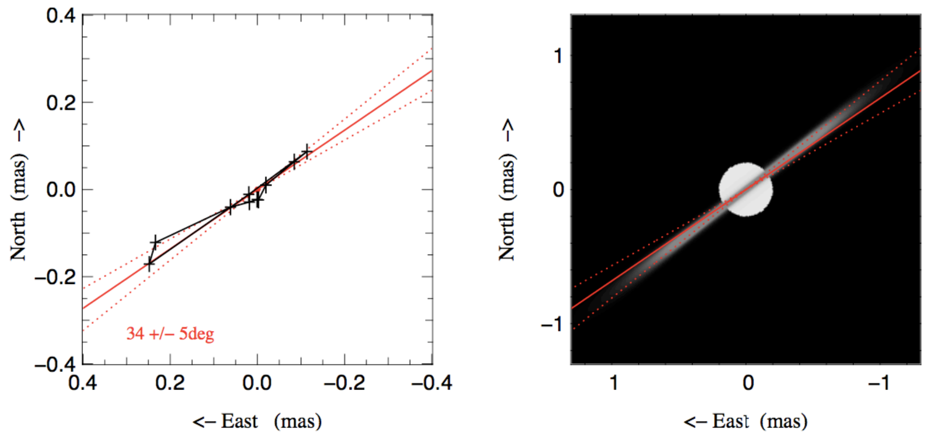

Fig. 13. Left: Photocenter shifts derived from the AMBER relative phases across Brγ. The maximum shift is about 0.4 mas within the plane of the circumstellar disk, while no significant offset perpendicular to it can be found (black line). Right: The position angle derived from our differential data overplotted on the model of Gies et al. (2007).

HR Differential measures: Betelgeuse

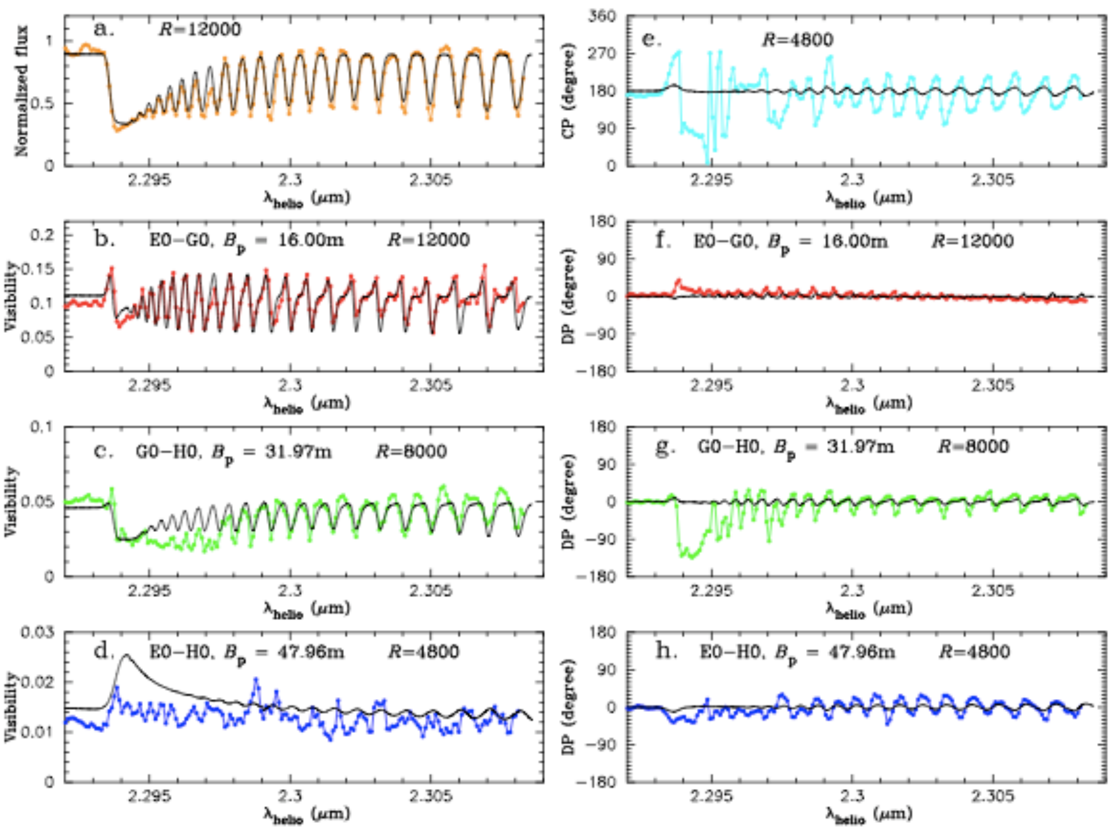

Fig. 5. Comparison between our patchy model (T_{in} = 2250 K, N_{out} = 1×10^{20} cm^{-2}, v_{flow} = 10 km s^{-1}, Θ = 60°, θ = 40°, and ϕ = 10°) and the AMBER data for Betelgeuse. In all panels, the solid lines represent the model, while the dots represent the observational data (data set #1). **a)**: Normalized flux. **b)–d)** Visibilities on the E0-G0-16 m, G0-H0-32 m, and E0-H0-48 m baselines. The observed and model visibilities on the last two baselines are binned with three and five pixels, respectively. **e)**: Closures phase. The observed data and the model are binned with five pixels. **f)–h)**: Differential phases on the E0-G0-16 m, G0-H0-32 m, and E0-H0-48 m baselines. The observed and model DPs on the last two baselines are binned with three and five pixels, respectively.

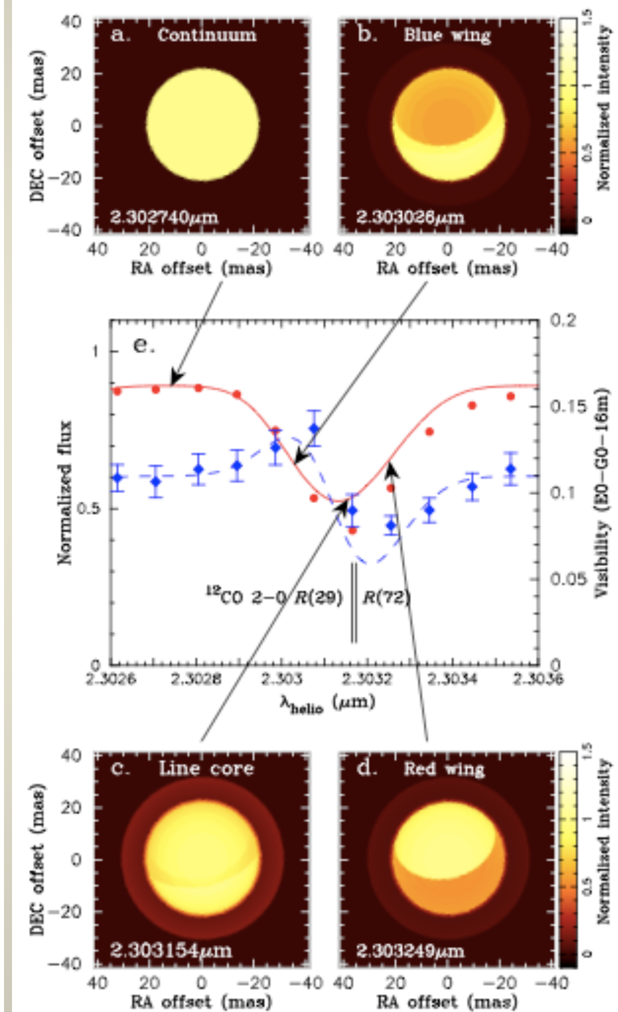

Ohnaka et al., A&A 2009

See also Ohnaka et al., A&A 2013 on Antares

The recurrent Nova T Pyx
a pole-on bipolar ejection

Chesneau et al.: The 2011 outburst of the recurrent nova T Pyx.

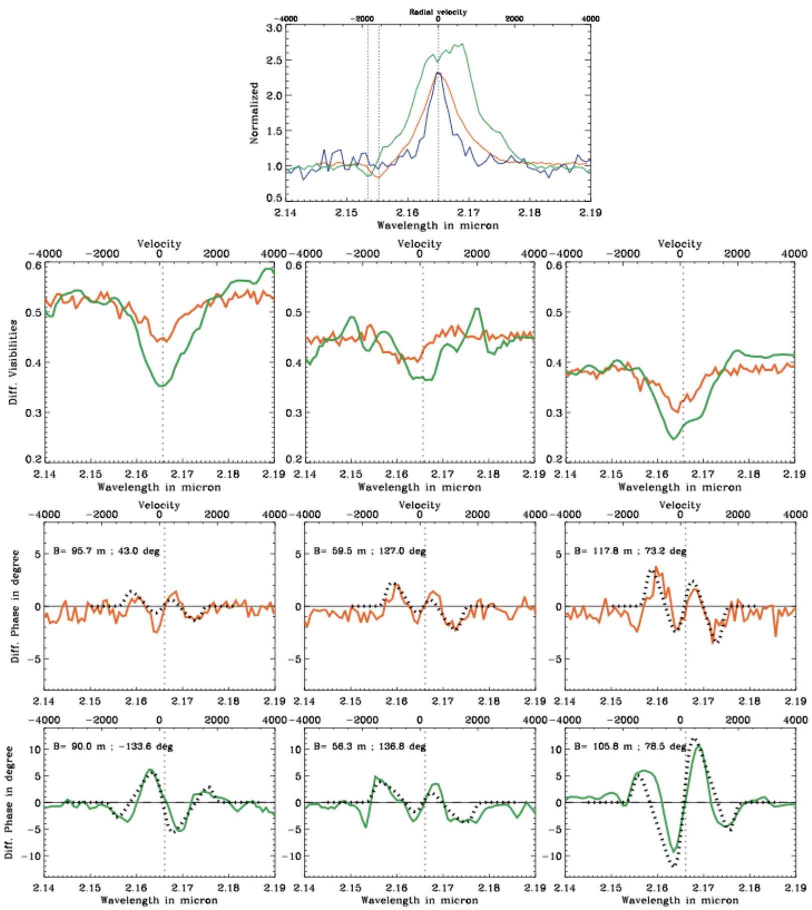

Fig. 5. AMBER data. Top: comparison between the Brγ line at t=8.81 (blue curve), t=28.76d (red curve) and t=35.77d (green curve). **Bottom**: Above - differential visibility comparison between t=28.76d and t=35.77d (scaled to the continuum V^2 at t=28.76). Below: same with differential phases. The phases are compared with the phases from the model (dashed line, χ_r^2=1.1 and 1.4, respectively).

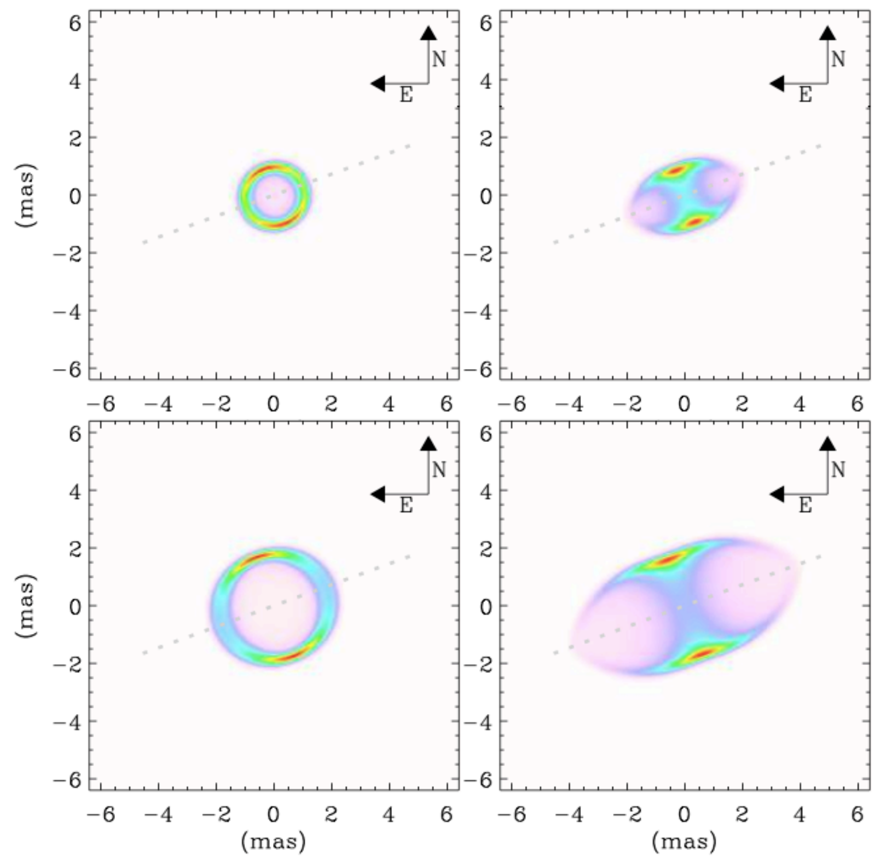

Fig. 6. Brγ Bipolar-flow model (without central source) seen at i=90° (right) and i=10° (left , the best model) and P.A.=110° (best model).

Chesneau et al., 2011

Global « image » of η Car wind

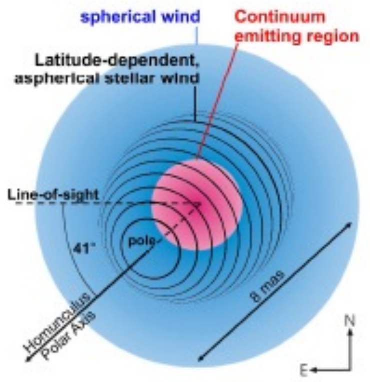

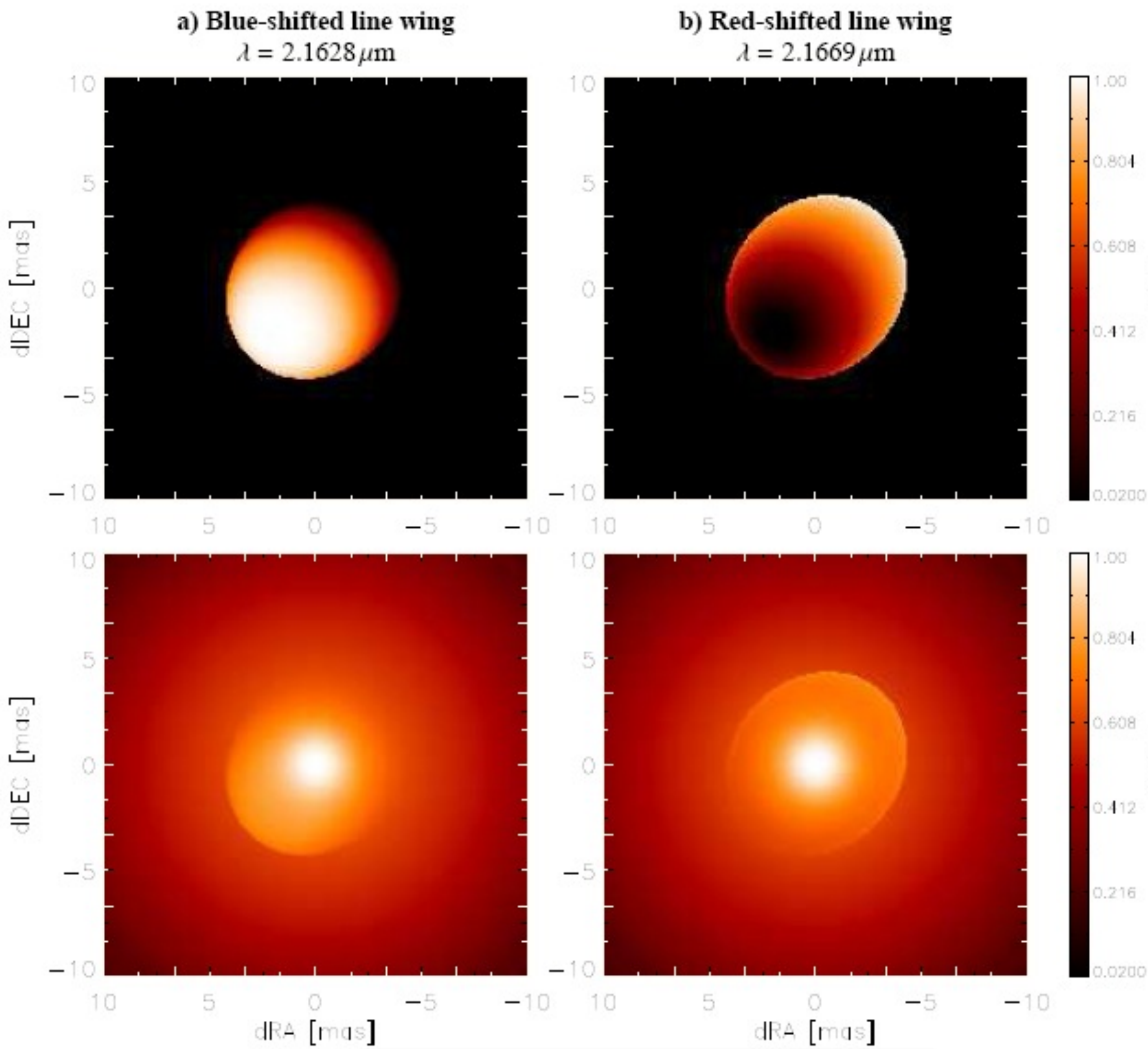

Fig. 10. **Top:** Illustration of the components of our geometric model for an optically thick, latitude-dependent wind (see text for details). For the weak aspherical wind component, we draw the lines of latitudes to illustrate the 3D-orientation of the ellipsoid. **Right (a, b):** The upper row shows the brightness distribution of the modeled aspherical wind component (item (3) in the text) for two representative wavelengths. The figures below show the total brightness distribution after adding the contributions from the two spherical constituents of our model.

Weigelt et al., 2011

Polychromatic Imaging using the differential phase.

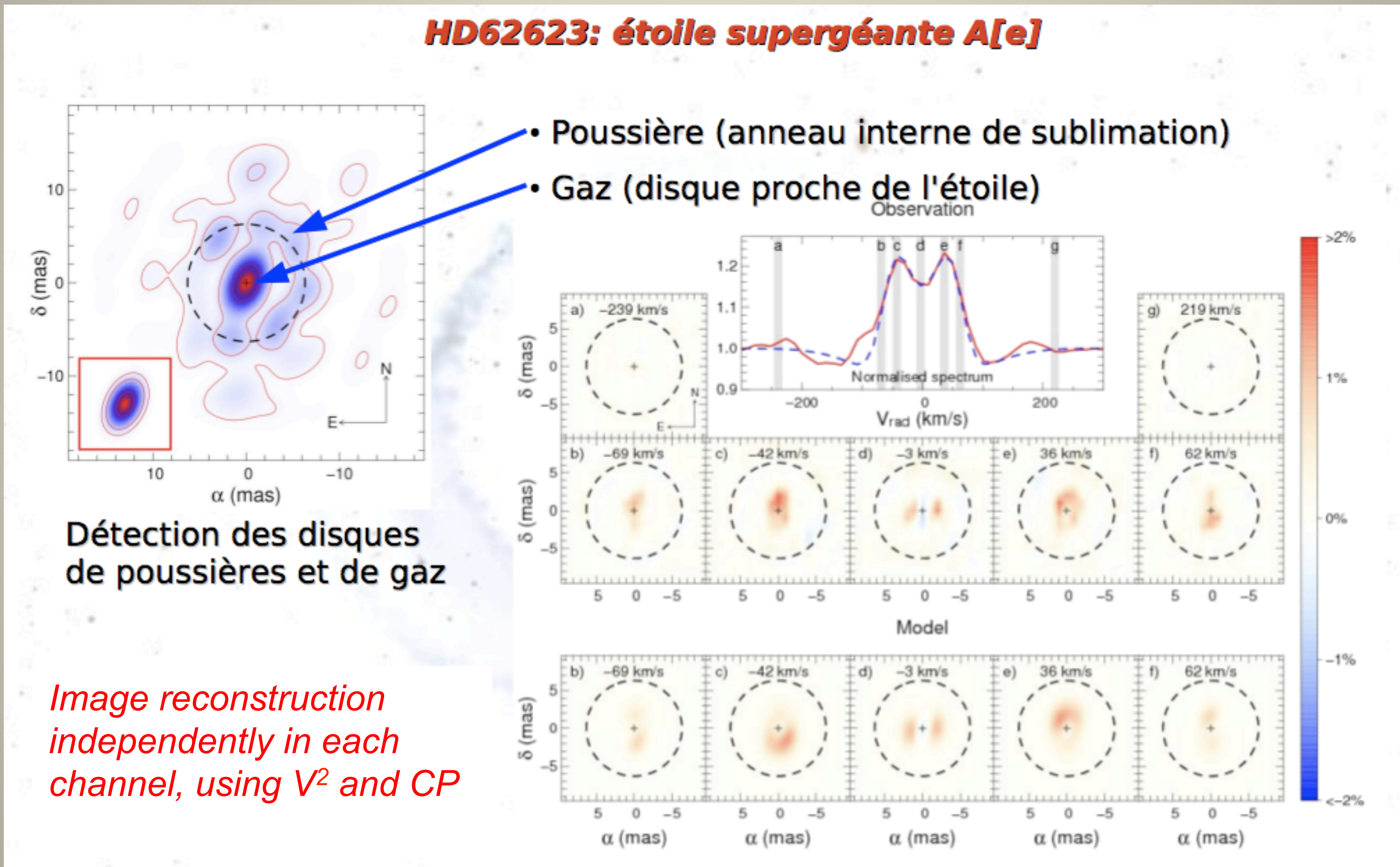

Polychromatic Imaging using the differential phase.

HD62623: étoile supergéante A[e]

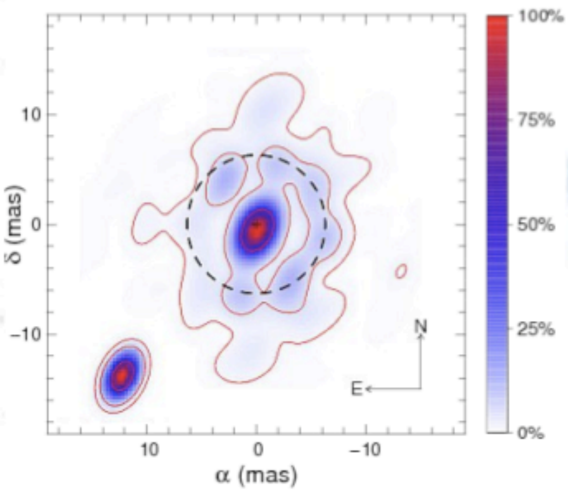

Étoile tourne à une vitesse proche de la vitesse critique

Polychromatic image reconstruction in the data cube using V², Differential phases and CP

"self-calibration" : phases différentielles dans la reconstruction d'images

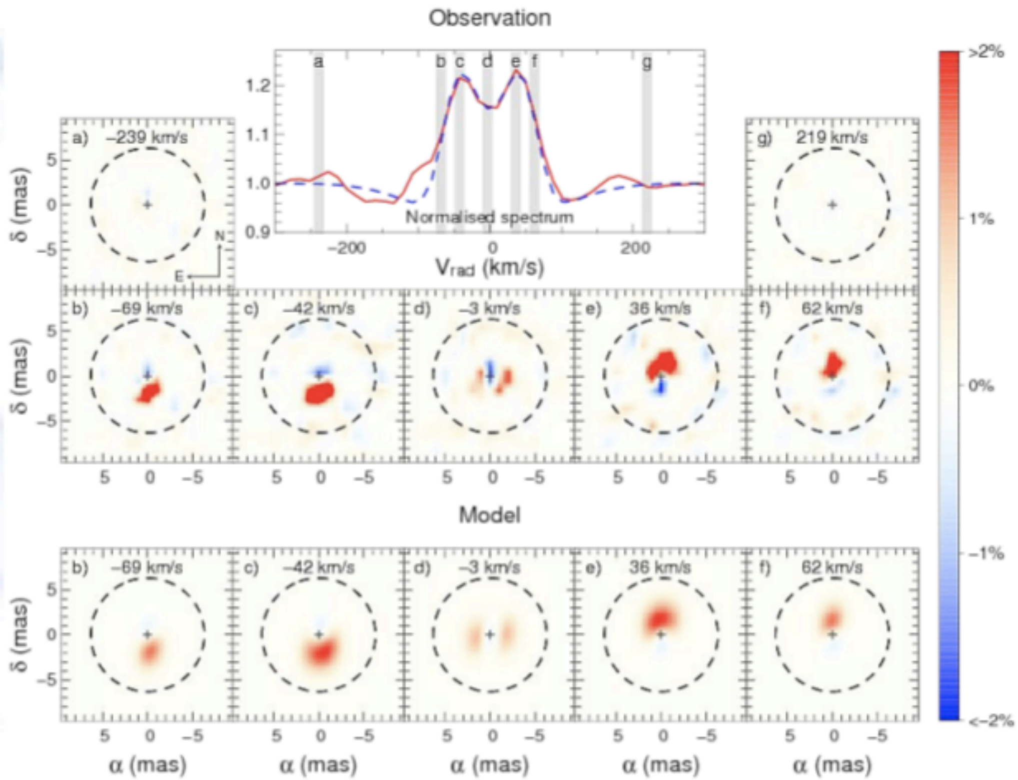

Millour et al., 2011

HD62623: dust disk and gas kinematics of an A[e] star

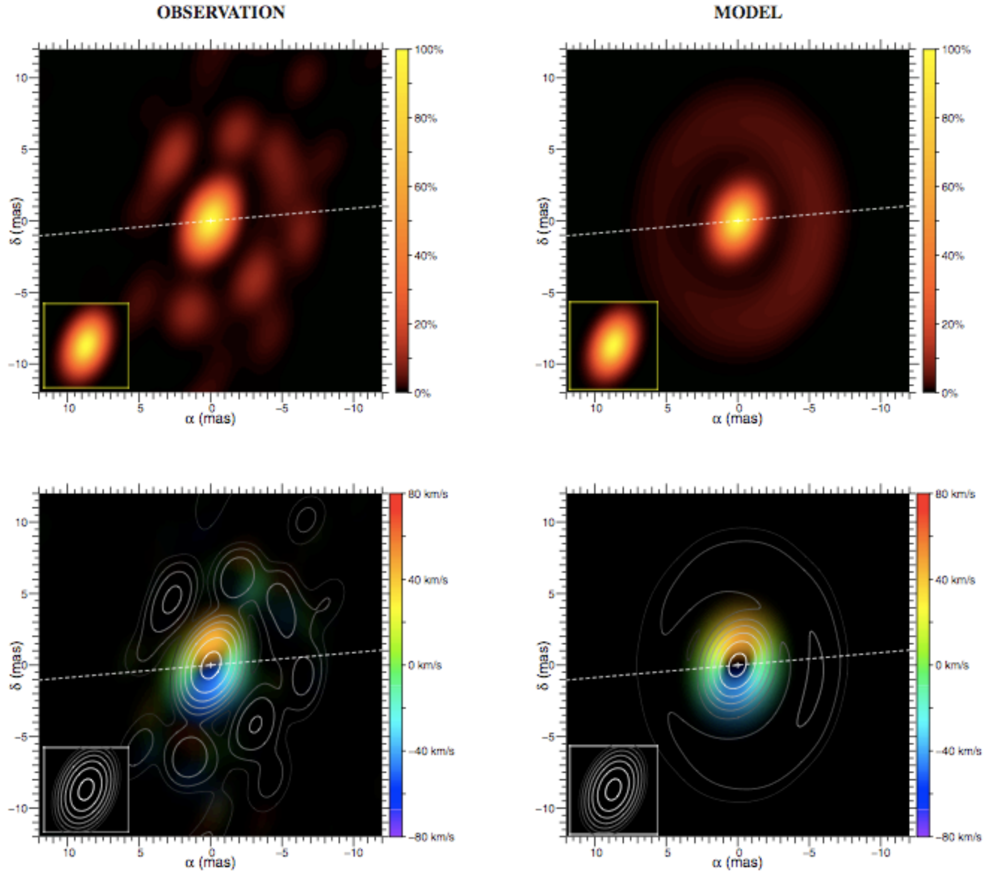

Fig. 4. *Top-Left*: composite aperture-synthesis image of HD 62623. The convolving beam of 1.75 × 2.76 mas is shown in the lower-left box at the same scale. The dashed line represent the polarization measurement from Yudin & Evans (1998). *Top-Right*: our best-fit model plot at the same scale and convolved with the same beam. *Bottom-left*: line images of HD 62623. The line intensity is plot as colours for different gas velocities. The intensity in the continuum is plot as gray contours (80%, 40%, 20%, 10%, 5%, 2.5% and 1.25% of the peak intensity). *Bottom-Right*: our best-fit model line images with the same representation and the same convolving beam.

Principle of self calibrated polychromatic imaging

Millour et al., 2011

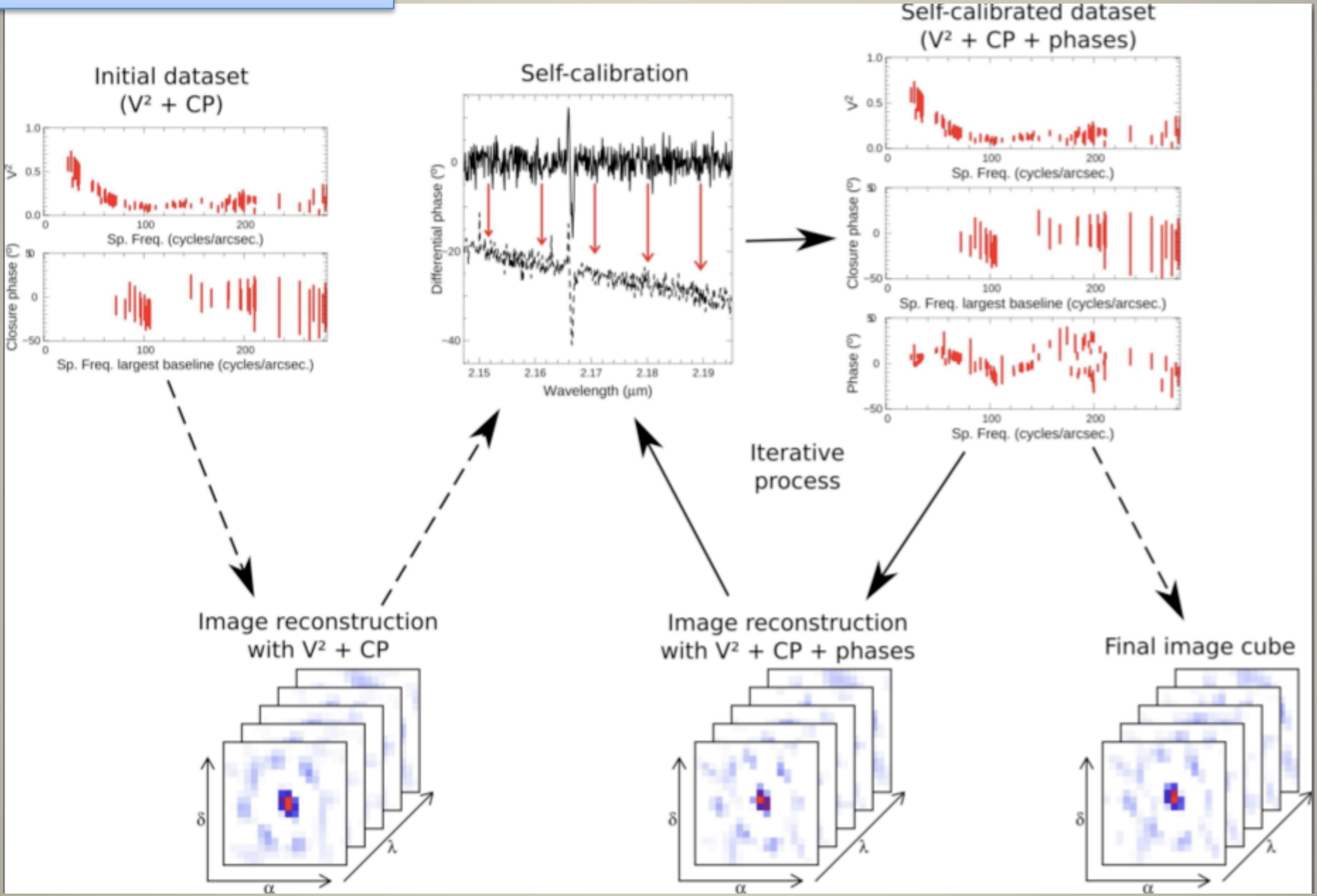

Photocenter displacements

- ESO CfP: 1°
- Unresolved source $\Phi<\lambda/B$
- Differential phase

$$\Phi(\lambda)=2\pi(B/\lambda)\varepsilon_B(\lambda)$$

  - with $\varepsilon_B(\lambda)$=photocenter displacement in the baseline direction (Petrov 1986 and 1988)
  - With B=100 m, 1° phase accuracy =10 μas displacement error.

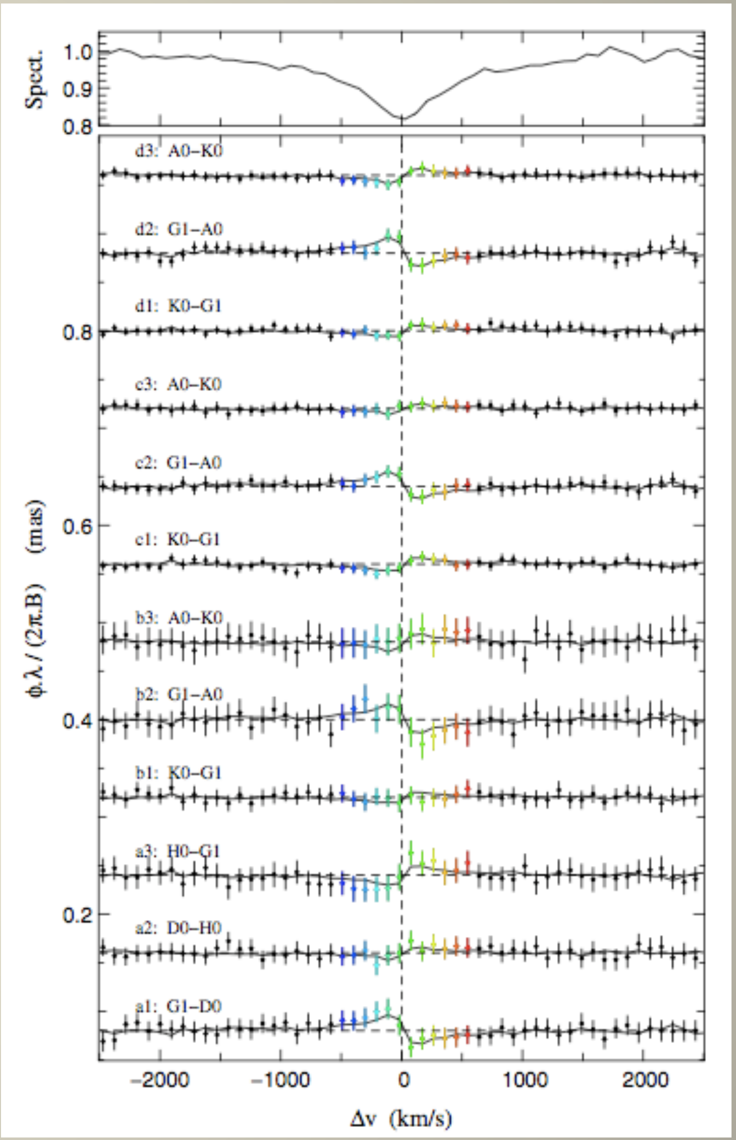

Photocenter displacements

L44 J.-B. Le Bouquin et al.: The spin-orbit alignment of Fomalhaut probed by OLBIN

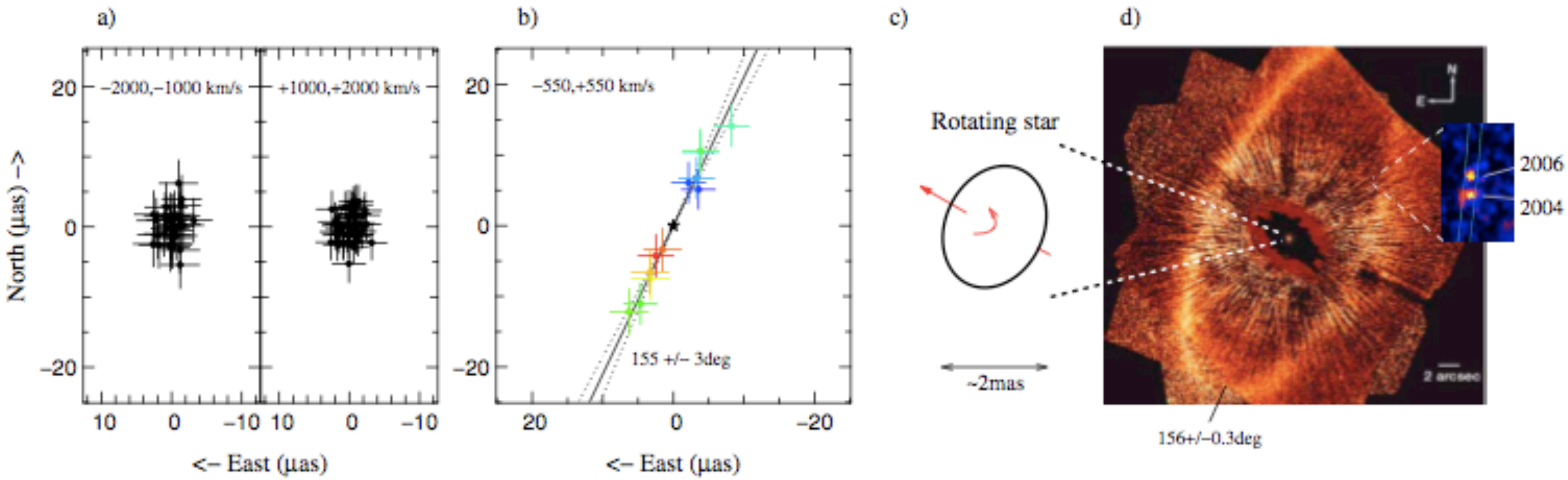

Fig. 3. AMBER spectro-astrometric positions $p(\lambda)$ in the continuum **a)** and across the Br-γ absorption line **b)**. Colors refer to the wavelength bin, as shown in Fig. 2. The signature of the rotating photosphere **c)** is clearly detected and is compared to the debris disk and the planetary companion **d)** imaged in the visible by Kalas et al. (2008). For the sake of clarity, the astrometric error ellipses are represented by their projection in the North and East directions.

Le Bouquin et al., A&A L 2009

Photocenter displacements

Chelli & Petrov, 1995

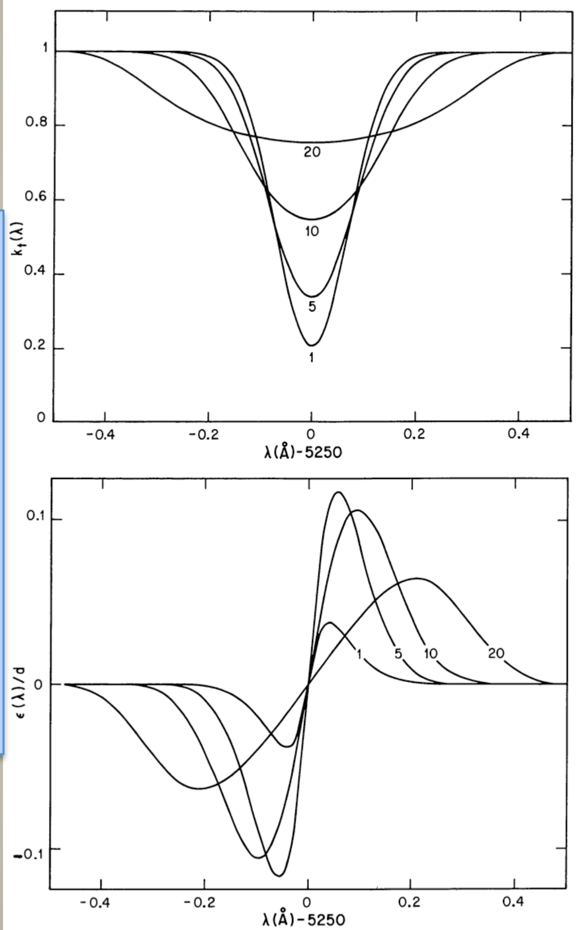

Fig. 1. Broadened line profile $k_t(\lambda)$ (a) and photocenter displacement in stellar diameter units $\varepsilon(\lambda)/d$ (b) for stars rotating as rigid bodies with equatorial velocities equal to 1, 5, 10 and 20 km/s. We assumed an infinite spectral resolution and a local line profile representative of a K star described by Eq. (22)

Domiciano et al, 2012

A. Domiciano et al.: Beyond the diffraction limit of optical/IR interferometers. I.

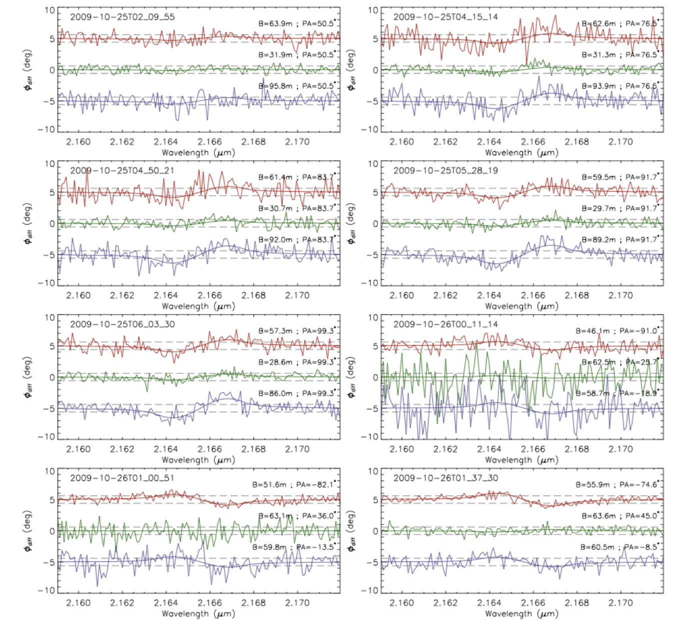

Fig. 5. The 84 VLTI/AMBER $\phi_{diff}(\lambda)$ measured on Achernar around Brγ at 28 different observing times (format YYYY-MM-DDTHH_MM_SS) and, for each time, three different projected baselines and baseline position angles, as indicated in the plots. The dashed gray horizontal lines indicate the median $\pm\sigma_\phi = \pm 0.6°$ of all observations. The smooth curves superposed to the observations are the best-fit ϕ_{diff} obtained with a uniform-rotation, gravity-darkened Roche model, as described in Sect. 4. All the observed ϕ_{diff} points are shown here, even if the fit has been performed using only each third wavelength point (cf. Sect. 4). All ϕ_{diff} curves are equal to zero in the continuum, but they were shifted for better readability. The other panels are available in the electronic edition.

Best-fit parameter	Best-fit value and error
Equatorial radius R_{eq}	$11.6 \pm 0.3\, R_\odot$
Equatorial rotation velocity V_{eq}	298 ± 9 km s^{-1}
Rotation-axis inclination angle i	$101.5 \pm 5.2°$
Rotation-axis position angle PA$_{rot}$	$34.9 \pm 1.6°$
Fixed parameter	**Value**
Distance d	44.1 pc
Mass M	$6.1\, M_\odot$
Surface mean temperature $\overline{T}_{eff}$	15 000 K
Gravity-darkening coefficient β	0.20
Derived parameter	**Value and error**
Equatorial angular diameter $\oslash_{eq}$	2.45 ± 0.09 mas
Equatorial-to-polar radii R_{eq}/R_p	1.45 ± 0.04
$V_{eq} \sin i$	292 ± 10 km s^{-1}
V_{eq}/V_{crit}	0.96 ± 0.03
Polar temperature T_{pol}	$18\,013^{+141}_{-171}$ K
Equatorial temperature T_{eq}	$9955^{+1\,115}_{-2\,339}$ K
Luminosity $\log L/L_\odot$	3.654 ± 0.028

Photocenter displacement, position-velocity diagram and mass estimates

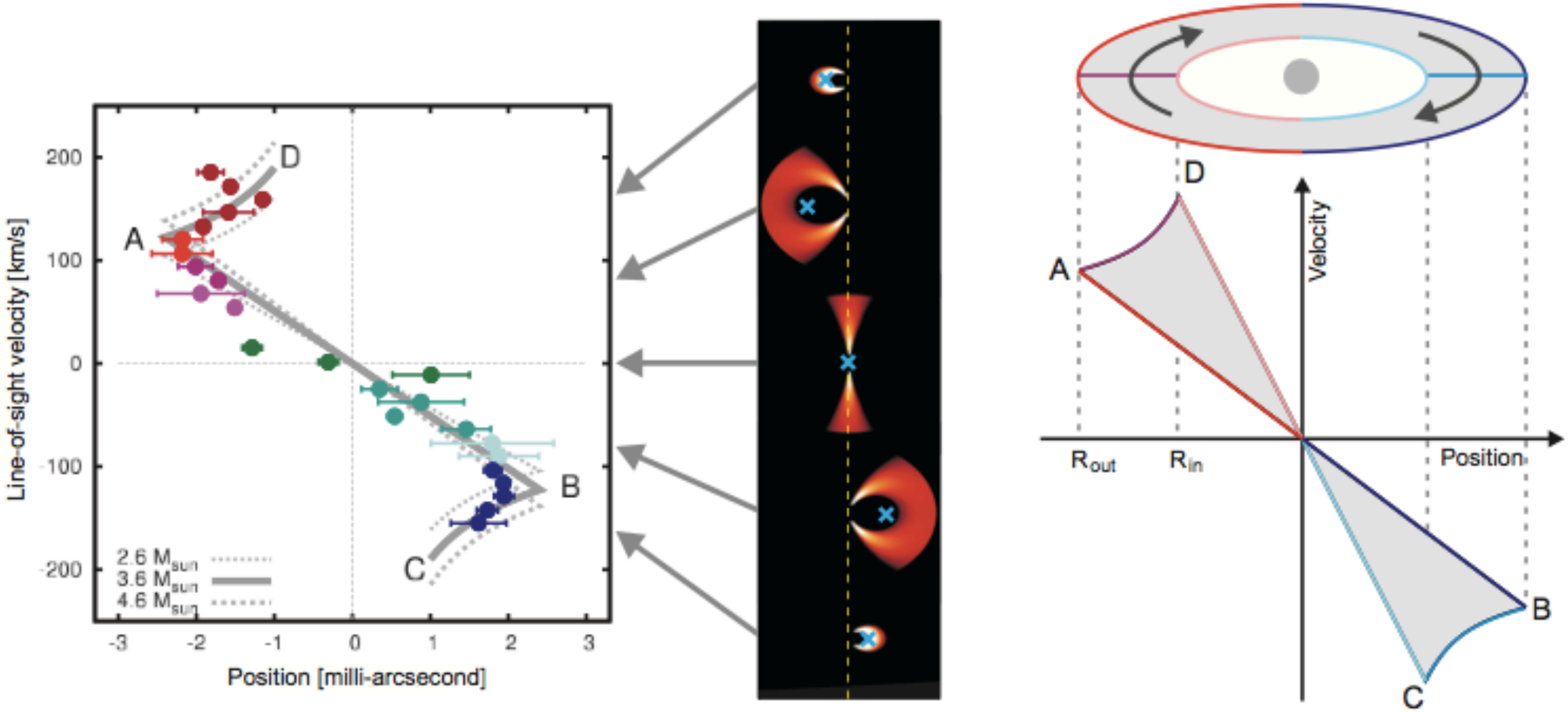

Figure 2. **Left:** Position-velocity diagram for β CMi, constructed from a single VLTI/AMBER observation with spectral dispersion $R = 12,000$. **Right:** Sketch, illustrating the "bowtie"-shaped structures, which appear in the position-velocity diagrams of Keplerian-rotating disks (see Sect. 2.2 for details).

Kraus et al., 2012

BLR observations

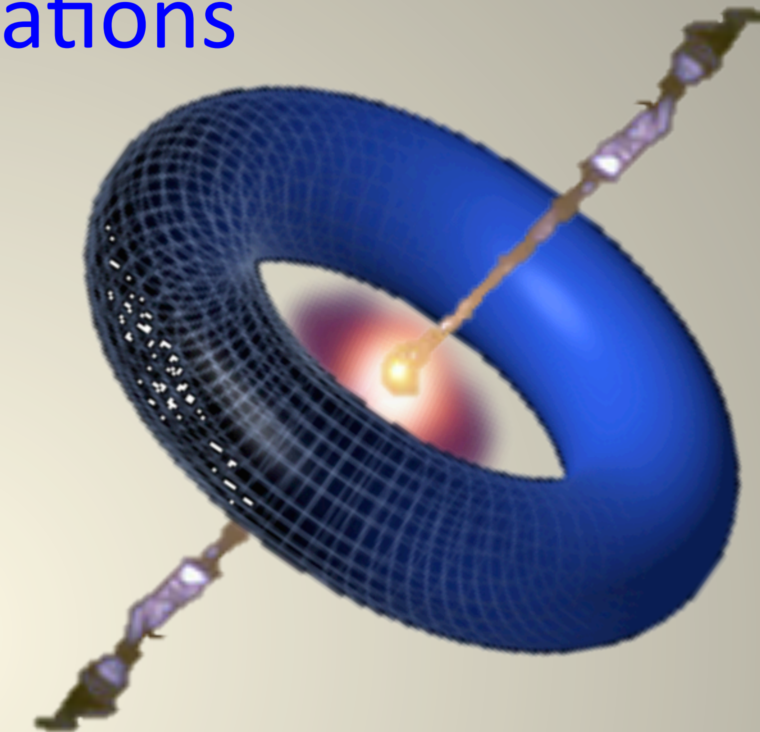

- Inflow-outflow around the SMBH
- Accurate Mass measurements
- Accretion rate estimation
- Calibration of Reverberation Mapping
  - Delay-Luminosity calibration
  - Size-Delay calibration
  - Mass-Luminosity calibration
  - Goal: use Sy1 and QSO as
    - **Standard candles**
    - **Standard Mass tags**
    - **Up to z~3**

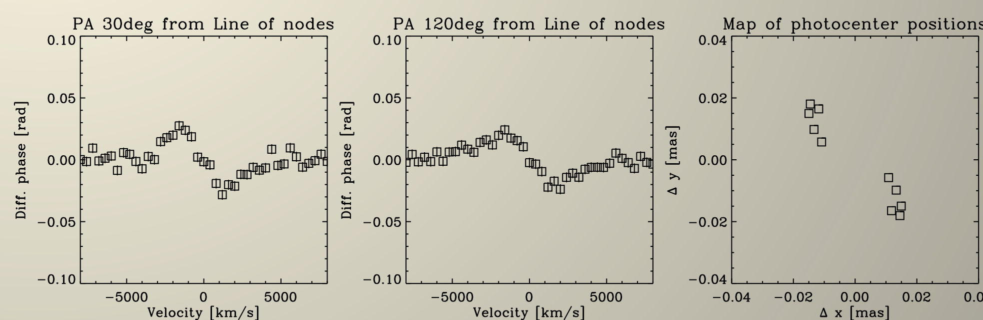

Blind mode observing and 2DFT processing

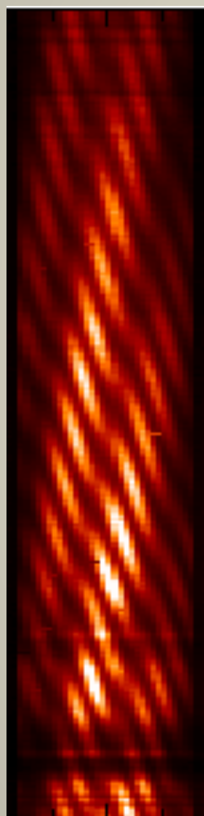

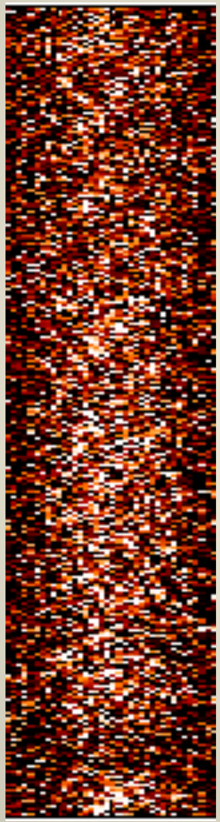

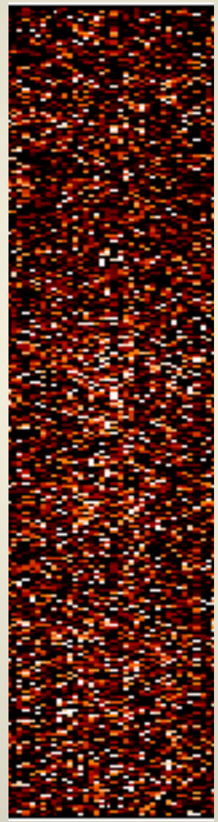

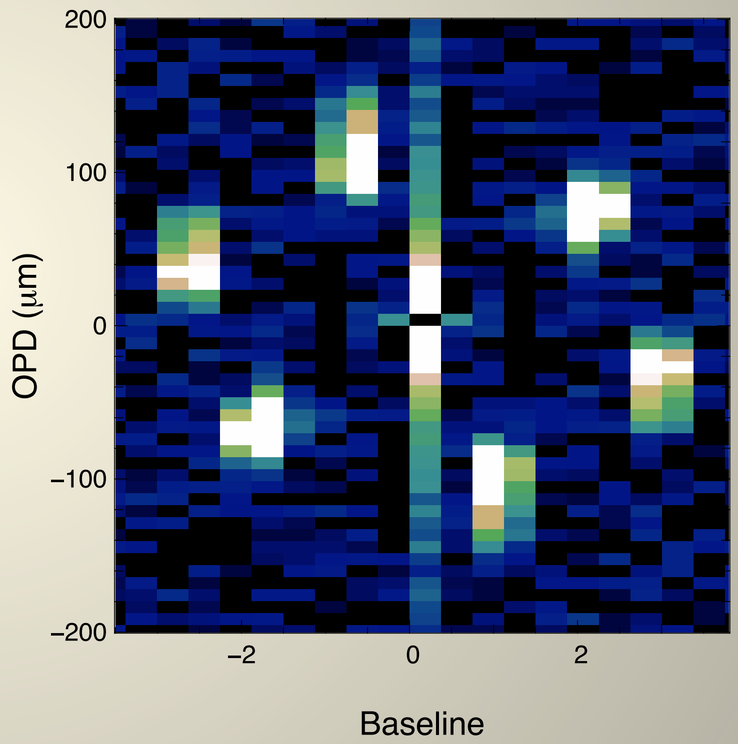

K=4 K=8.5 K=10 3C273 fringe peaks (10 s)

3C273 results

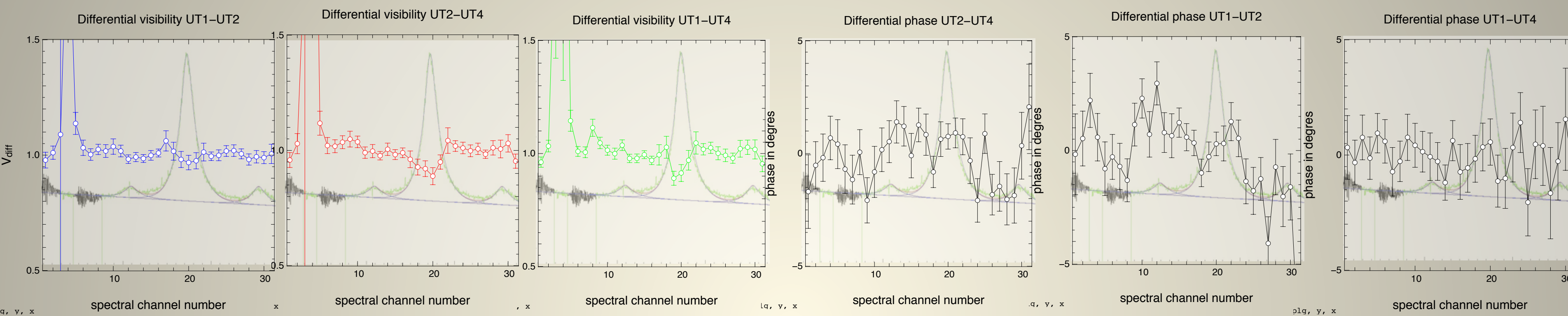

- Differential visibility (equivalent width)

$$\frac{V_{line}(50m)}{V_{cont}(50m)} = 0.98 \pm 0.03, \quad \frac{V_{line}(80m)}{V_{cont}(80m)} = 0.94 \pm 0.04, \quad \frac{V_{line}(125m)}{V_{cont}(125m)} = 0.92 \pm 0.04$$

The BLR gas extends beyond the inner dust rim

Radius (FWHM)= 0.5±0.1 mas (1500±500 ld)

Contradicts RM radius: 400±150 ld

- Differential phase

$$\Phi = 0 \pm 1.5°$$

Petrov et al, SPIE 2012

Reverberation Mapping bias

- With the 3C273 observing span (2000 days), Reverberation Mapping gives only a lower limit of the actual BLR radius

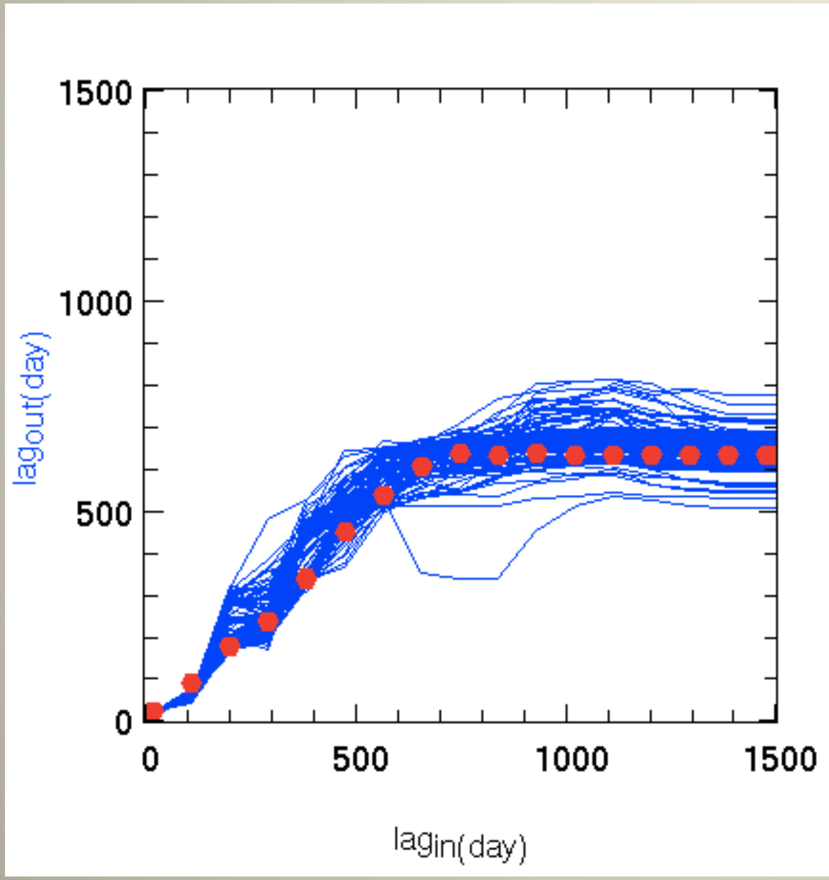

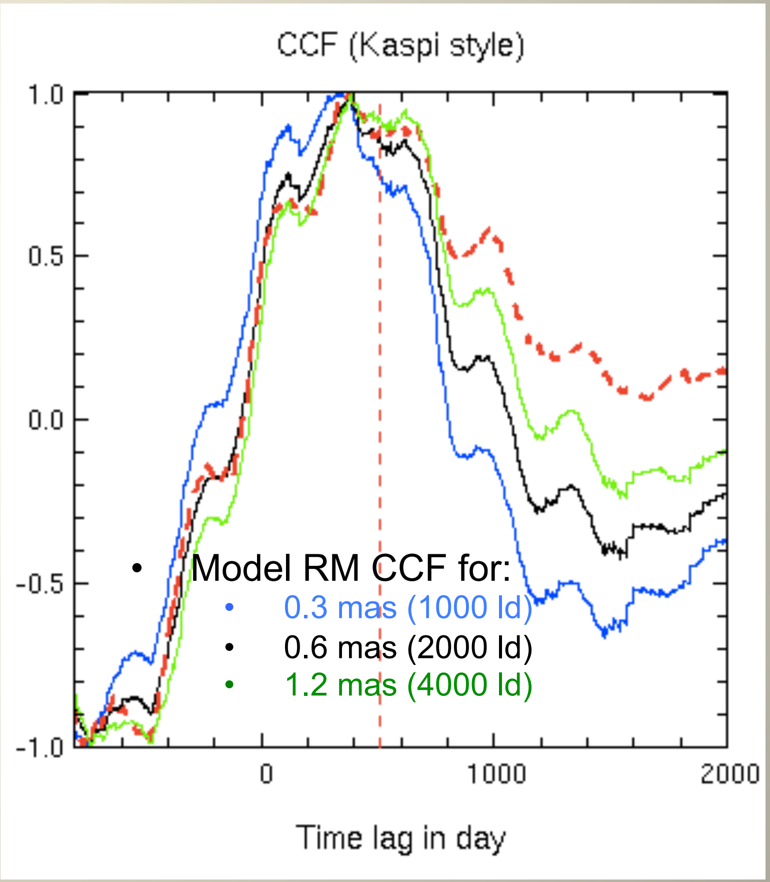

Rakshit et al, 2014

3C273 modeling

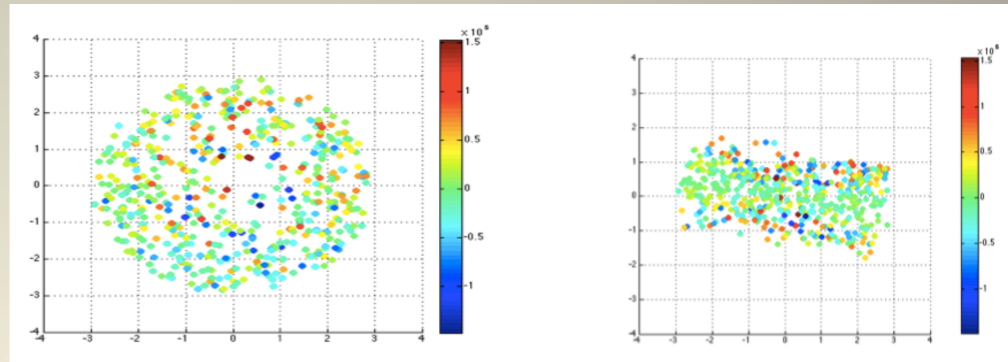

- Radius (FWHM): 0.5±0.1 mas
  (1500±500 ld)

  Kaspi (2000):

  $R_{BLR}=307_{-91}^{+69}$ ld = 0.10 mas in H_γ

  $R_{BLR}=514_{-65}^{+64}$ ld = 0.16 mas in H_α

- Inclination: 17±5°
  - From Jet models (i>10° and i<30°)
- Opening angle: $\omega>60°$
- Global Keplerian + local turbulent velocity
  - $<V_{kep}>\sin i=2000\pm300$ km/s
  - $<V_{turb}>=1000\pm300$ km/s
- Mass = 6±2 10^8 M_{sun}
  - (Kaspi 2000: 2 10^8 M_{sun} ,
  - Paltani 2005: 60 10^8 M_{sun})

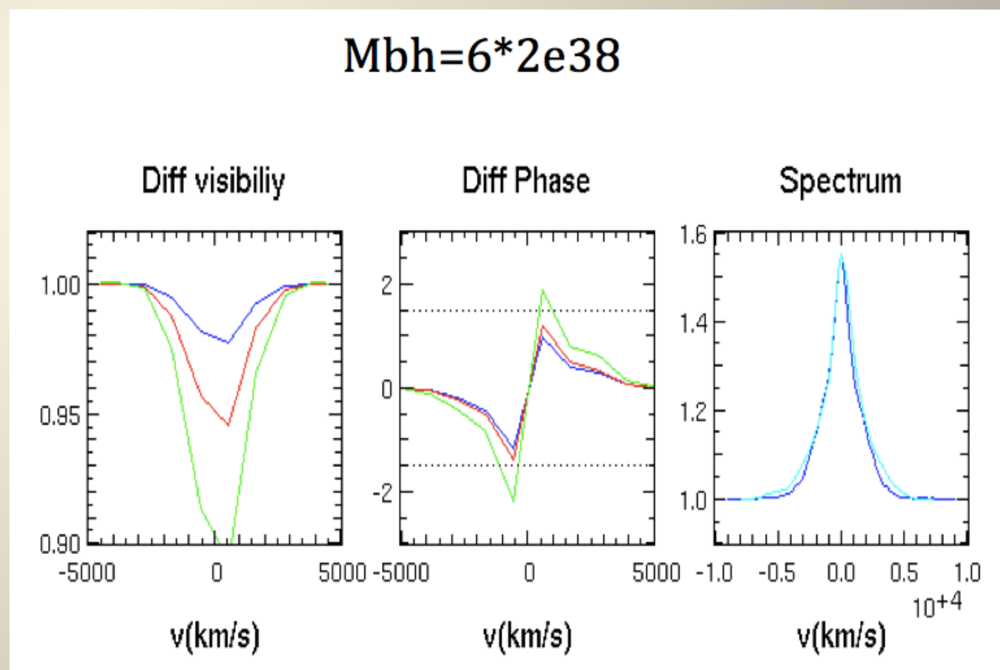

Petrov et al, 2014

What can still be improved

- All measures at MR and HR are ~ fundamental noise limited at the current AMBER or FINITO sensitivity
- Visibility accuracy: from 3-5% to ~1% using FINITO data
- CP in LR: from a few ° to 0.1°-0.3° using piston noise calibration
- Differential phase LR: from a few ° to 0.1° through careful differential OPD calibration
- Limiting magnitudes:
  - From 8-9 (P2VM) to 10-11 (2DFT)
  - From 10-11 to 12-13 using a specific module or a new spectro-interferometric instrument

Conclusion

- **AMBER has been and still is the most productive interferometric instrument ever**
- AMBER has produced its share of LR observations, including images
  - Accuracies in LR are insufficient although there are possible strong improvements
  - In LR, PIONIER then GRAVITY make AMBER obsolete
- The most valuable contributions are spectro-interferometric
  - The differential measures at MR and HR are close to fundamental noise accuracy
  - Differential phase has a strong potential for super-resolution
  - Polychromatic imaging has a strong potential
  - The limiting magnitude in MR and HR has been strongly improved by 2DFT processing
  - It is possible to gain 2-3 more magnitudes. Such an improved AMBER will remain more sensitive in MR than GRAVITY and its internal FT
- AMBER/VLTI has continuously improved but
  - Data processing and procedure improvements propagate very slowly
  - Learning curve might has been slow
- **AMBER in MR and HR should be maintained in H&K and extended in J**
  - AMBER will remain more sensitive than GRAVITY with its internal Fringe Tracker
  - A specific spectro-interferometric would be of high interest
    - See “magnitude talk” tomorrow
  - In the J band, we gain a factor 2 in resolution and there are many lines of interest

Additional slides

BLRs: a program for high magnitudes in MR

1 h of observation, R=1500

X : differential phase from R_{in} diameter (IR reverberation mapping, extrapolated)

O : differential phase from RM radius (H_{β} RM extrapolated)

* : differential visibility from R_{in} and $R_{BLR} << R_{in}$

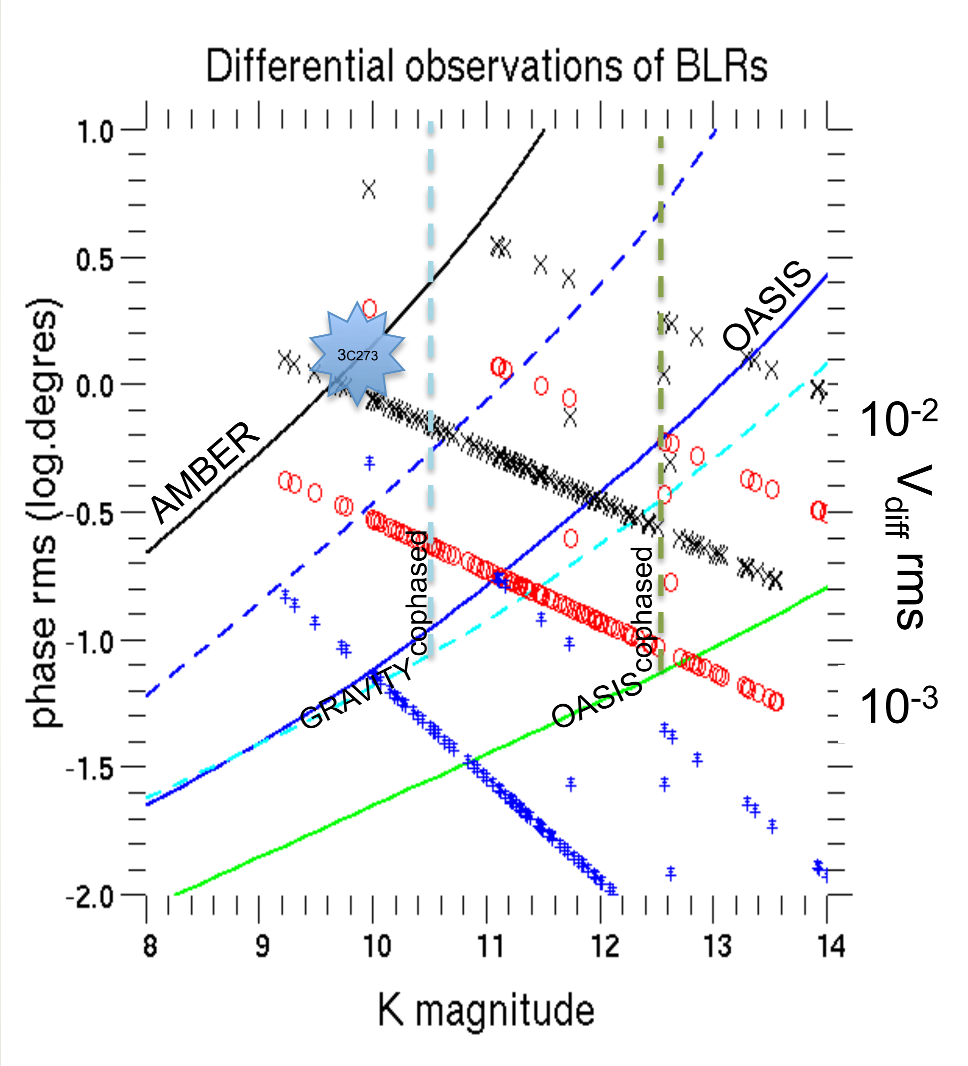

BLR observations: 3C273

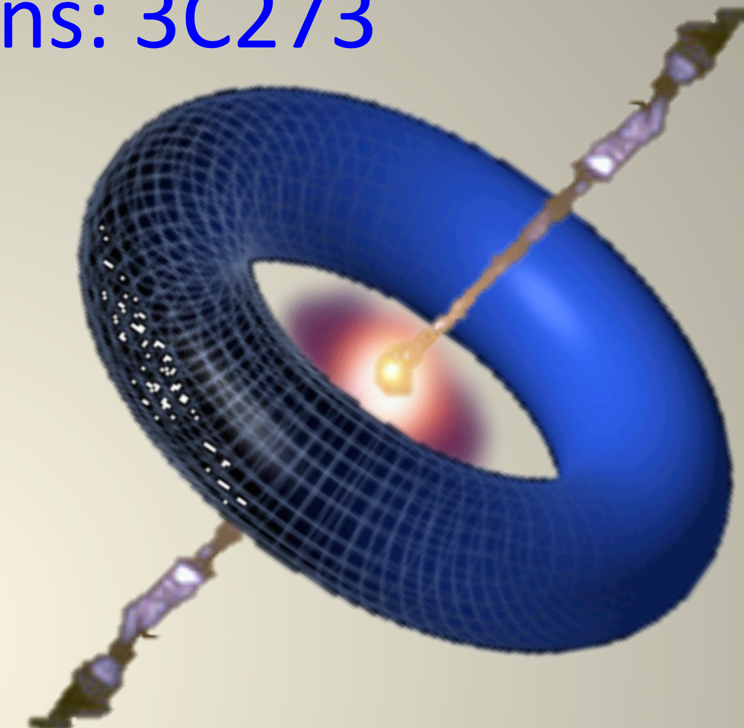

- Brightest QSO, K=9.7
  - K=9.8 in continuum; K=9.2 on top of line
- z=0.16
  - Pa_{α} line at 2.17 microns
- Reverberation mapping radius (Kaspi, 2000)
  - $R_{BLR}=307_{-91}^{+69}$ ld = 0.10 mas in H_{γ}
  - $R_{BLR}=514_{-65}^{+64}$ ld = 0.16 mas in H_{α}
- M_{BH}~2 10^8 M_{sun} (Kaspi, 2000)
  - ~60 10^8 M_{sun}, (Paltani, 2005)
- Radius of inner rim of torus
  - $R_T \approx 0.81\pm0.34$ pc=0.30 ± 0.12 mas (Kishimoto 2011)
- Absolute visibility
  - in continuum: $V \approx 0.93$ (from 0.95 on KI by Kishimoto 2011)
  - In line: $V\approx 0.96$ (from line Pa_{α} intensity)
- Differential visibility increase ~ 3%
- Differential phase perpendicular to axis
  - $\max[\Phi(\lambda)] \approx 40$ mrad (2°)
  - $\mathrm{Max}[\varepsilon(\lambda)] \approx 20$ μas
- Differential phase in axis direction
  - Up to inner radius ≈ 0.5 rad (300 μas)

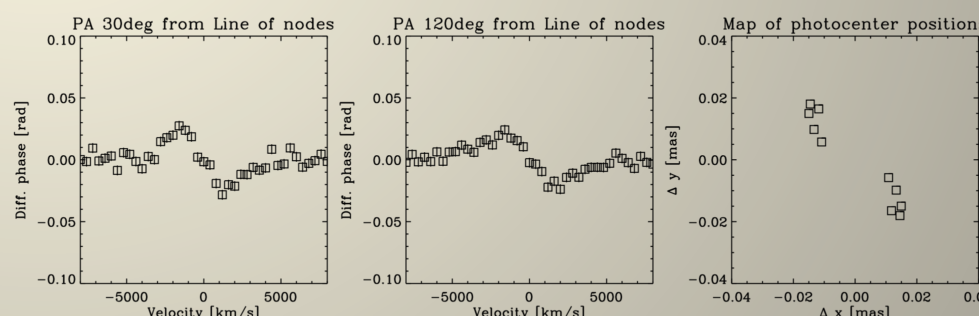

Reverberation mapping

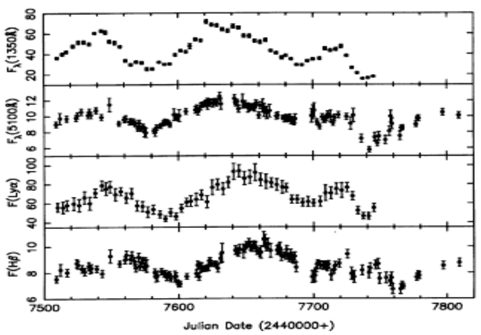

FIG. 4—Sample light curves for NGC 5548 from the 1988–1989 International AGN Watch monitoring campaign. Shown are the fluxes in the ultraviolet continuum (Clavel et al. 1991), the optical continuum (Peterson et al. 1992), the Lyα emission line (Clavel et al. 1991), and the Hβ emission line (Peterson et al. 1991). The continuum fluxes are in units of 10^{-15} ergs s^{-1} cm^{-2} Å^{-1}, and the emission-line fluxes are in units of 10^{-13} ergs s^{-1} cm^{-2}.

$$M_{\rm BH} = \frac{f r \Delta V^2}{G}$$

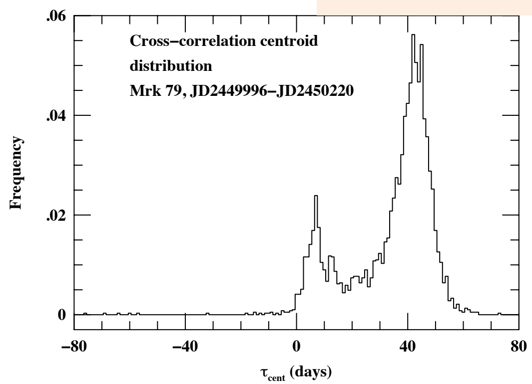

Fig. 11.— Cross-correlation centroid distribution for the continuum–Hβ cross-correlation for Mrk 79 during the period JD2449996 to JD2450220. It is not obvious which peak corresponds to the correct lag.

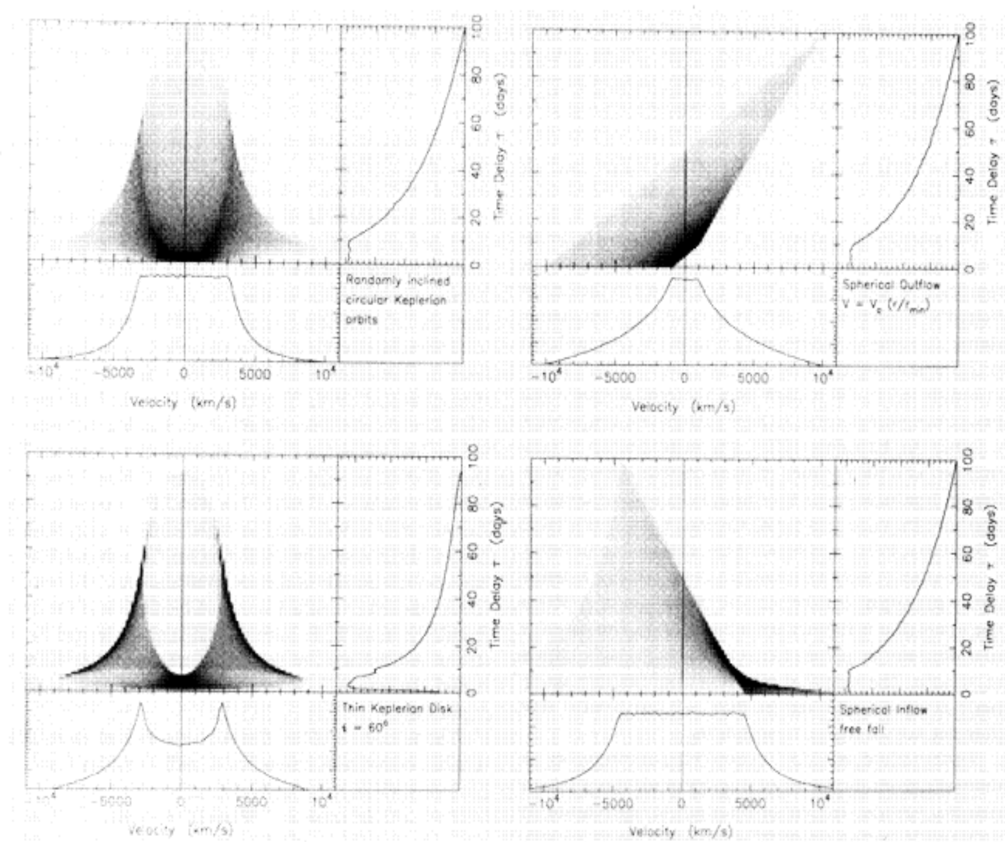

FIG. 8—Examples of two-dimensional echo images, from Welsh and Horne (1991), for various BLR geometries and velocity fields. The upper left panel of each image shows the two-dimensional transfer function as a gray-scale image in the velocity-time-delay plane. The one-dimensional transfer function $\Psi(\tau)$ is obtained by integrating over velocity, and this is shown in the upper right panel of each image. The line responsivity profile is obtained by integrating over time delay, and this is shown in the lower panel for each image. Despite having radically different geometries and/or velocity fields, the four examples shown here have very similar one-dimensional transfer functions; the two-dimensional transfer function would be required to distinguish among these possible models. Figure courtesy of W. F. Welsh.

Type 1 AGNs

(Makoto Kishimoto et al., 2014)

- About 15-20 sources accessible to current interferometry
  - K~11 (Keck I, VLTI/AMBER)
  - 0.2 Jy (VLTI/MIDI)
- Baseline up to 130m
  - Resolution 4 mas in K band
    - In K band, flux dominated by inner rim of dust torus (1500 K)
    - Tori marginally resolved: equivalent **ring radius**
  - Resolution 15 to 20 mas in N band
    - In N band, flux is dominated by thermal emission of Torus
    - Fairly resolved structure, it is possible to fit a radial distribution
    - We define **half-light radii**, corresponding typically
      - to 800 K at 8 μm
      - To 350 K at 12 μm

Type 1 AGN (Kishimoto 2014) R_{int}/R_{RM}

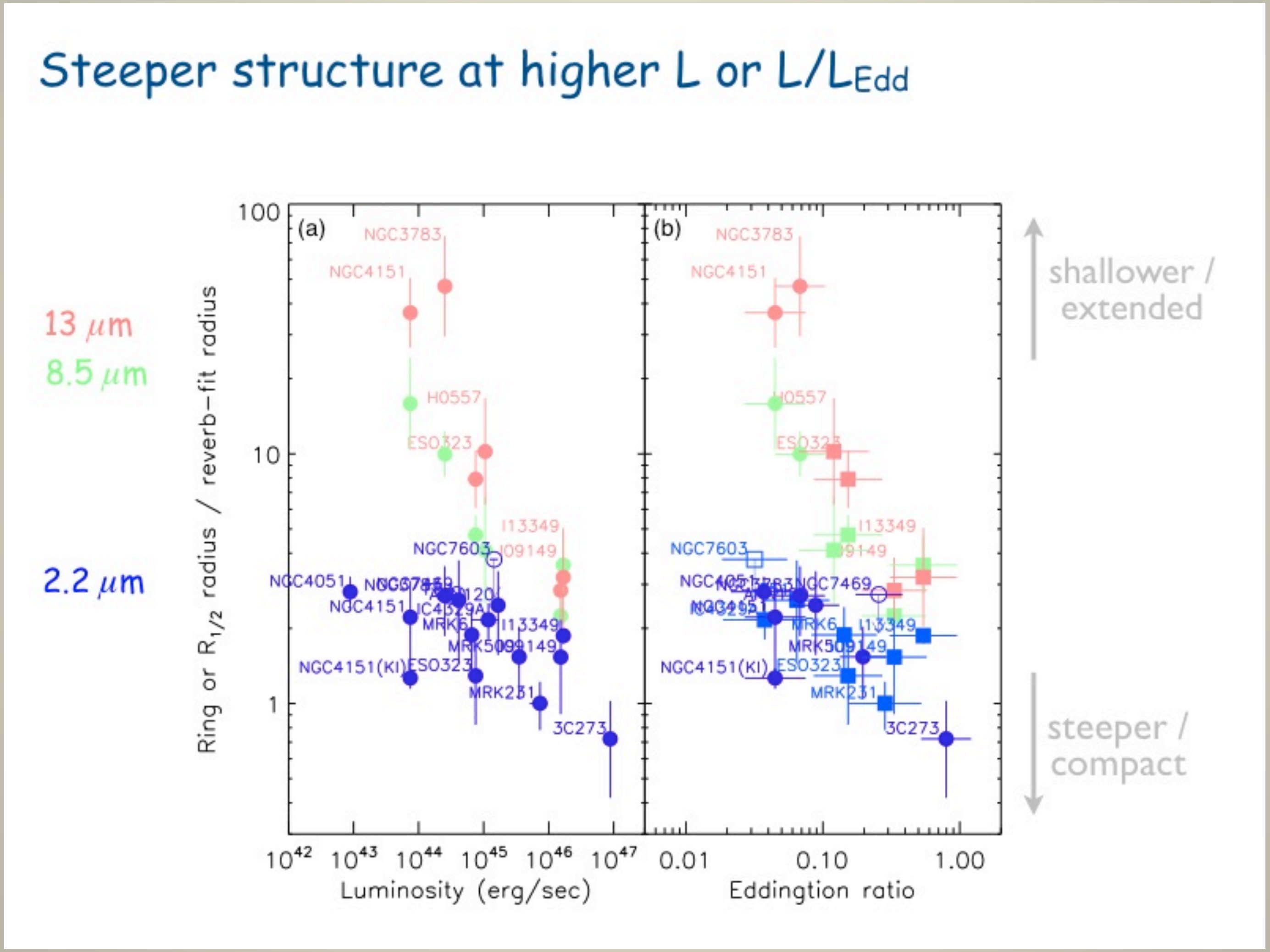

Type 1 AGN (Kishimoto 2014)
Steeper / Shallower structure

Steeper / shallower structure

- normalize by R_{in}, removing $L^{1/2}$ scaling
- representative radius in units of R_{in}

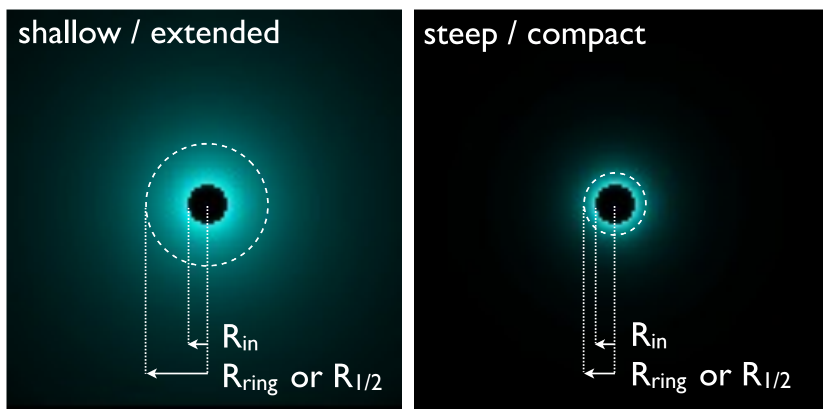

$R / R_{in} \gg 1$ $\qquad$ $R / R_{in} \sim 1$

Type 1 AGN (Kishimoto 2014)
Possible picture

- nIR/mIR - direct illum.
- Lower acc.rate:
  - eff. polar flaring, generally extended
- Higher acc.rate:
  - polar region cleared, equatorial steep struct.

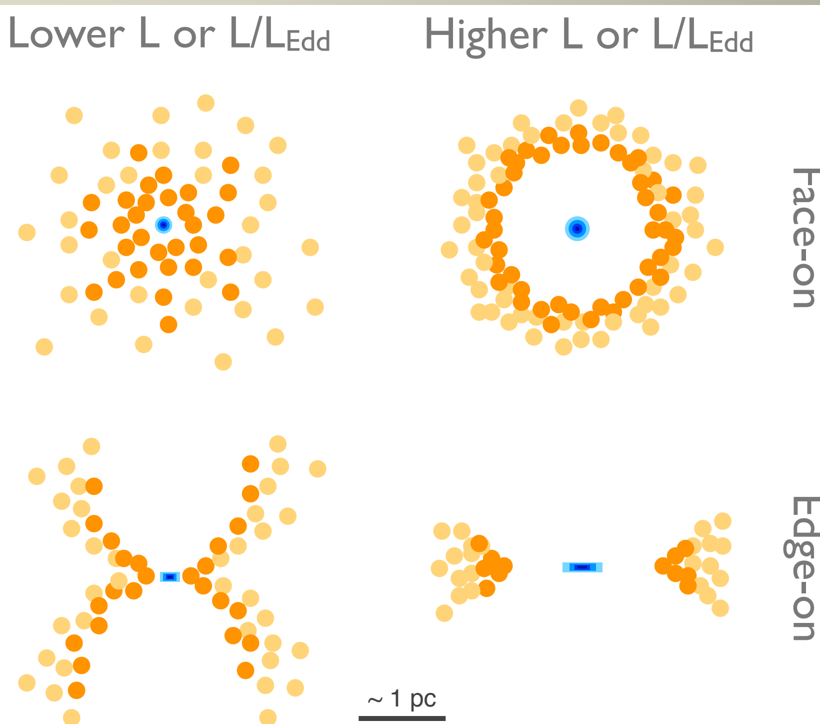

- Intrinsically steeper str. required for higher acc. rate?

Summary for AGN dust tori observations with AMBER

- Exploration of innermost dusty structure at mas resolution is on-going, both in the near-IR and mid-IR.
- The current sample indicates steeper structure at higher L or L/L_{edd}, i.e. higher accretion rate/efficiency.
- Possible, direct observational support for radiation pressure playing a key role in shaping the structure.
- Accurate phase-closure measurements now possible, leading to real mapping soon, or with MATISSE.
- VLTI can now observe down to K~11.5, with good AO.

Low Spectral Resolution H&K Multi monochromatic imaging VX Sgr

Cool late type star, type discussed.

Strong size variation with wavelength

Hot spots, max contrast in H

Extended molecular layers (water dominant) at 2 and 2.35-2.5 microns

Conclusion: closer too MIRA type

Confirmation of image features by model fitting:

Image="objective" detection of features

Model="extracting parameters" from features

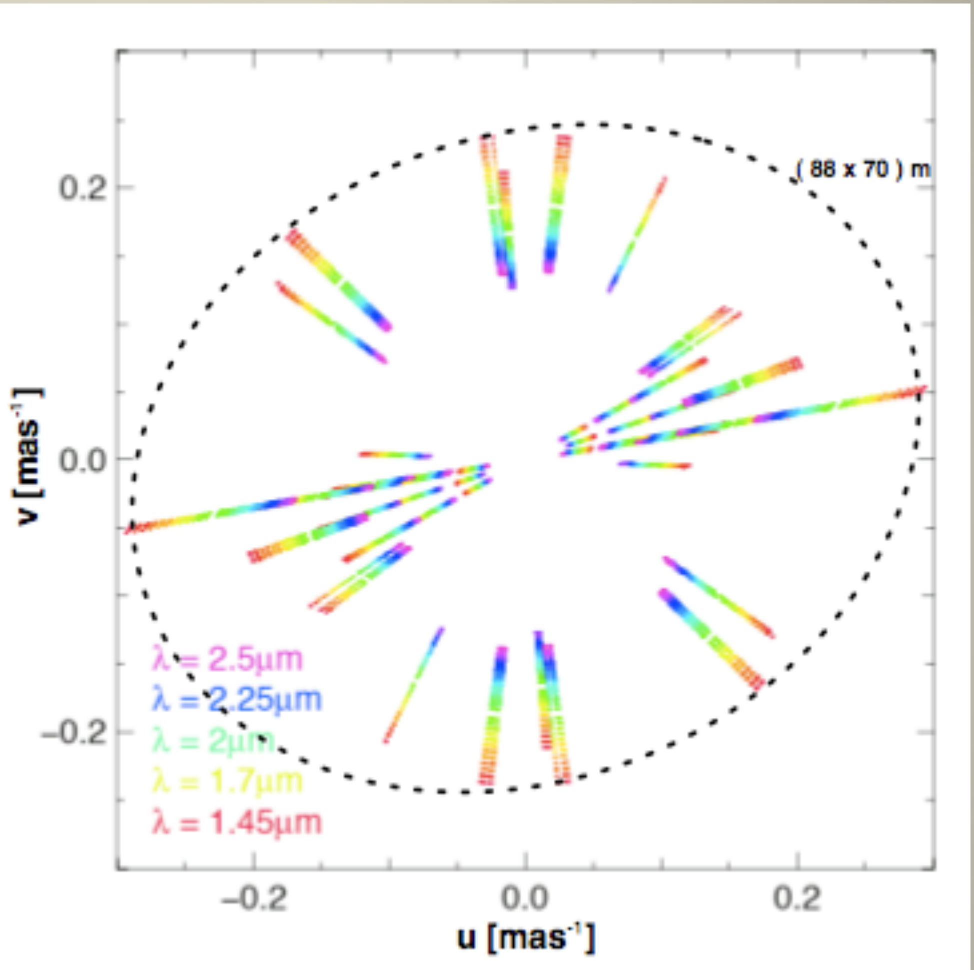

Low Spectral Resolution H&K Multi monochromatic imaging VX Sgr

Cool late type star, type discussed.

Strong size variation with wavelength

Hot spots, max contrast in H

Extended molecular layers (water dominant) at 2 and 2.35-2.5 microns

Conclusion: closer too MIRA type

Confirmation of image features by model fitting:

Image="objective" detection of features

Model="extracting parameters" from features

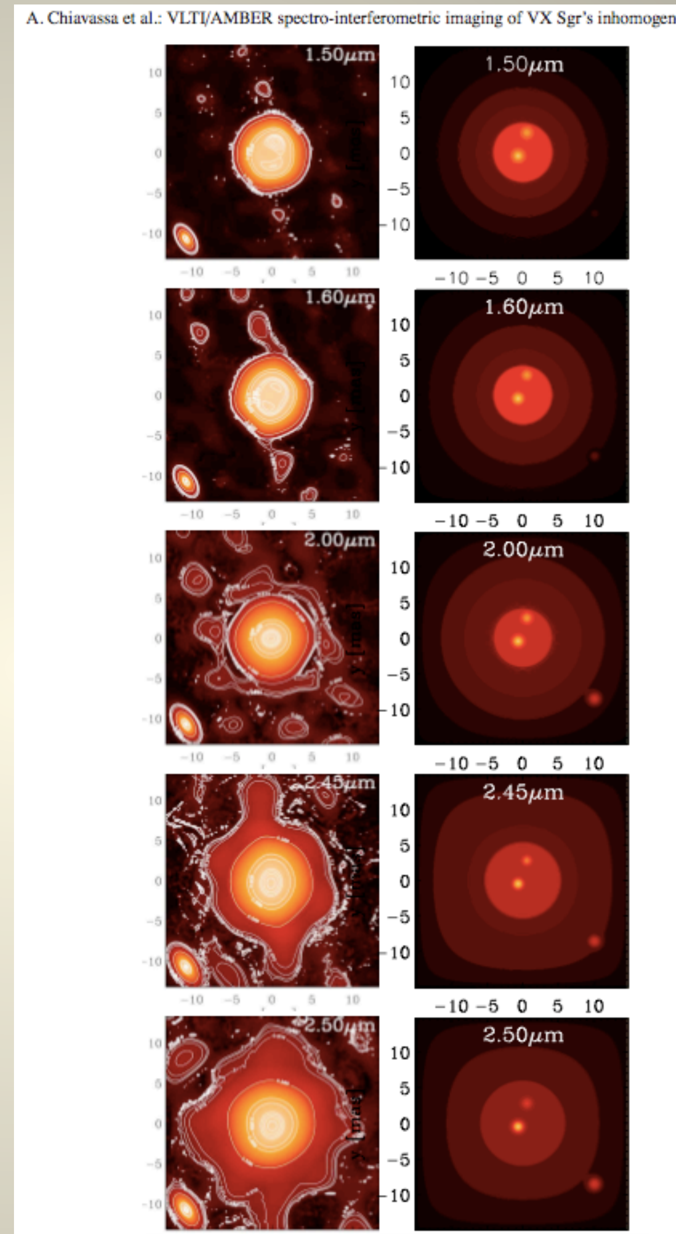

Chiavasa et al., A&A 2009

Low Spectral Resolution H&K Multi monochromatic imaging VX Sgr

Cool late type star, type discussed.

Strong size variation with wavelength

Hot spots, max contrast in H

Extended molecular layers (water dominant) at 2 and 2.35-2.5 microns

Conclusion: closer too MIRA type

Confirmation of image features by model fitting:

Image="objective" detection of features

Model="extracting parameters" from features

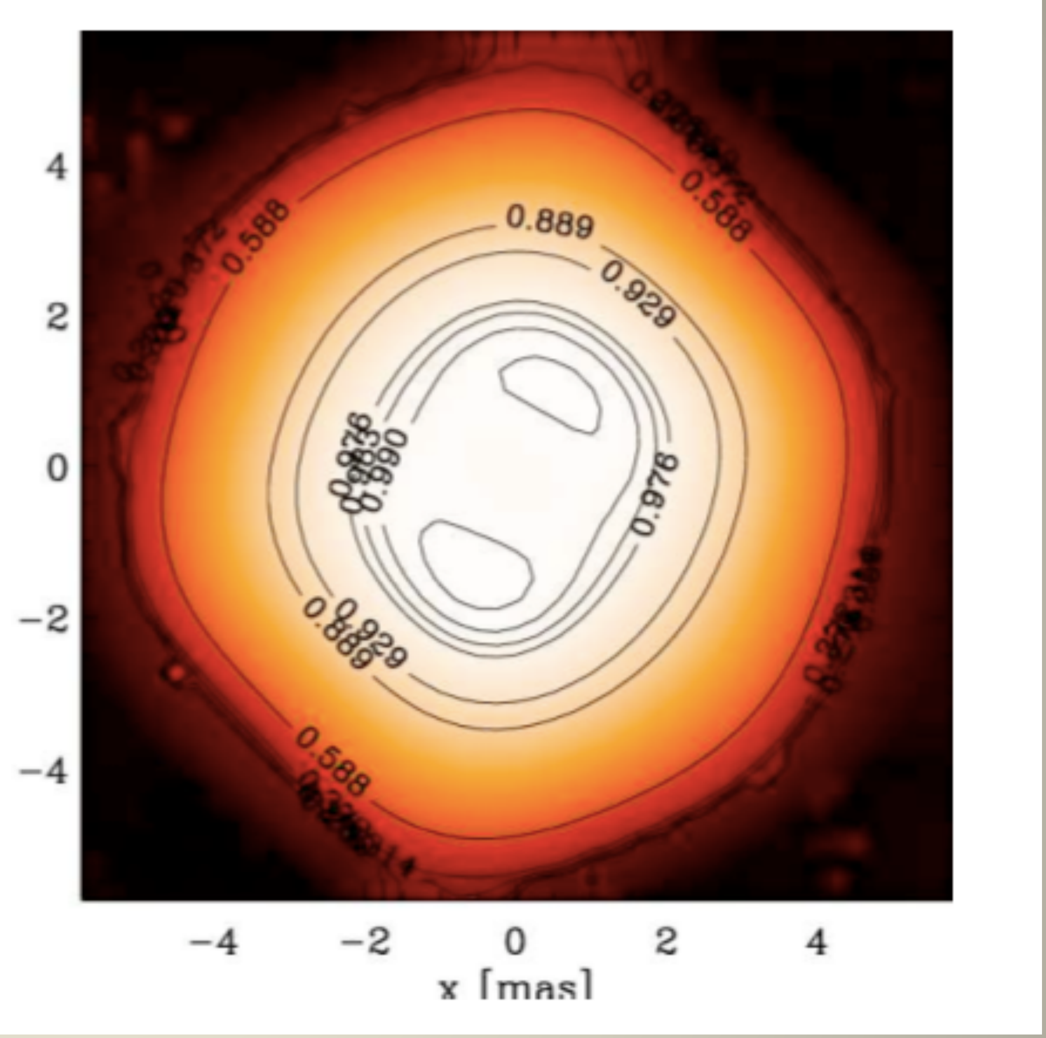

Chiavasa et al., A&A 2009

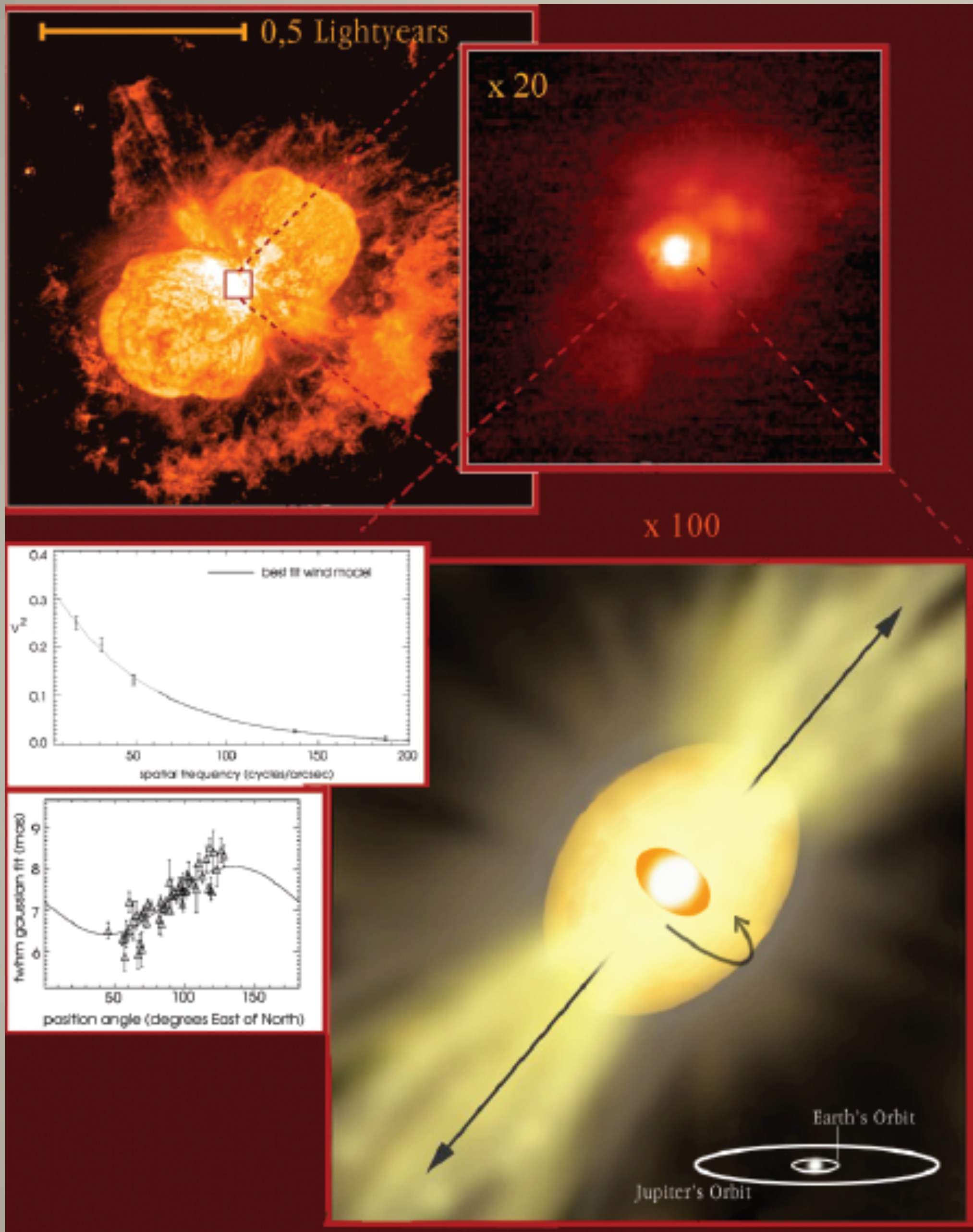

η Carinae

- L = 5 x 10^6 Lsun
- dM/dt = 5 x 10^{-3} Msun/yr
- 500km/s wind
- 60% of flux in the core of the AO image
- Contamination in single mode fibers evaluated from NACO images
- VINCI data resolves the central core: 5 mas (10AU)
- elongated along the flow axis

Fit of Differential and Closure Phase

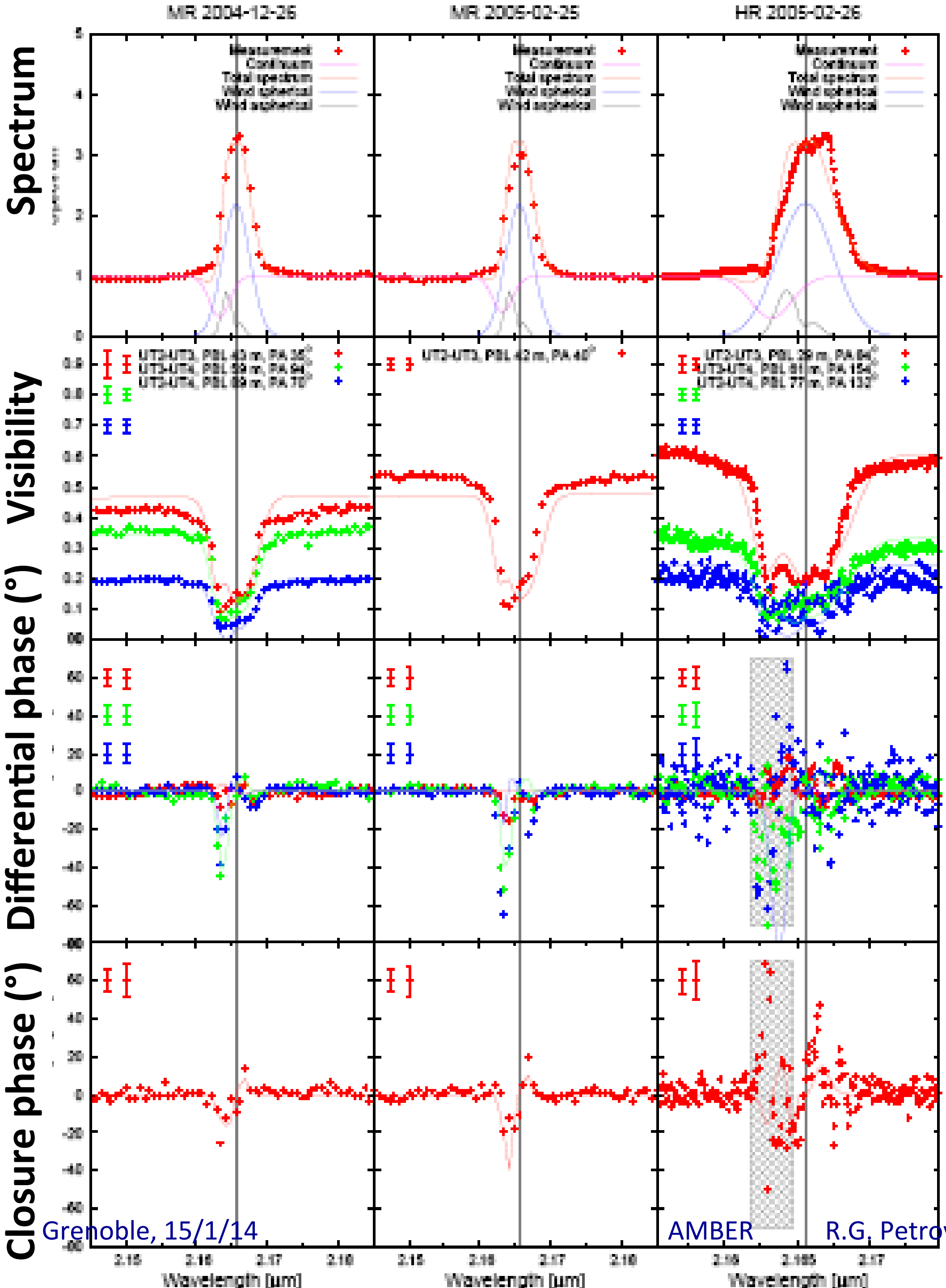

Global « image » of η Car wind

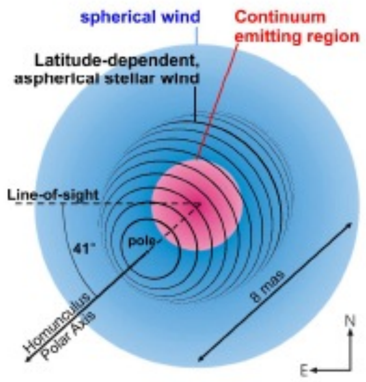

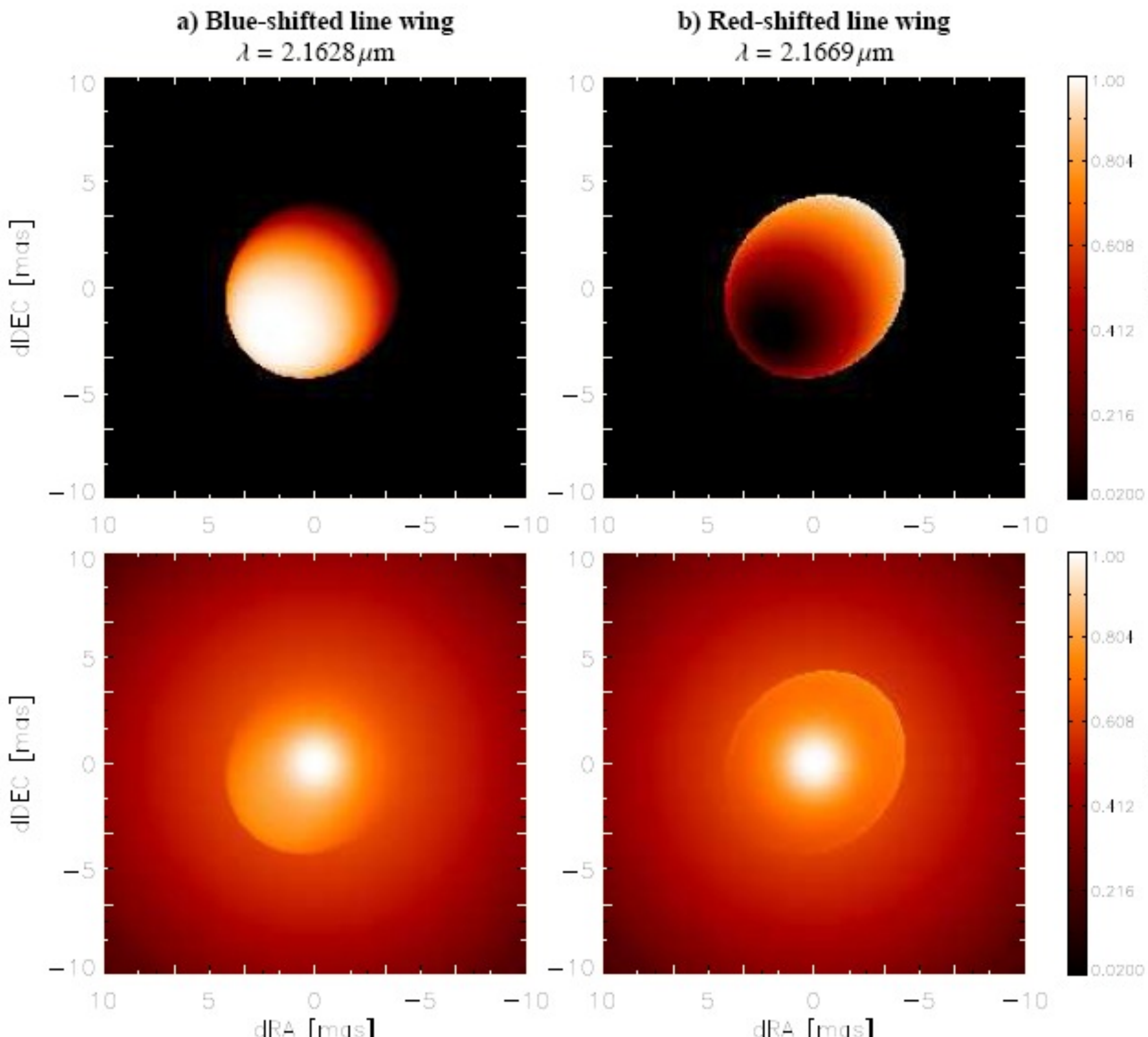

Fig. 10. Top: Illustration of the components of our geometric model for an optically thick, latitude-dependent wind (see text for details). For the weak aspherical wind component, we draw the lines of latitudes to illustrate the 3D-orientation of the ellipsoid. **Right (a, b):** The upper row shows the brightness distribution of the modeled aspherical wind component (item (3) in the text) for two representative wavelengths. The figures below show the total brightness distribution after adding the contributions from the two spherical constituents of our model.

Weigelt et al., 2011

Science topics in accepted publications
(January 2010)

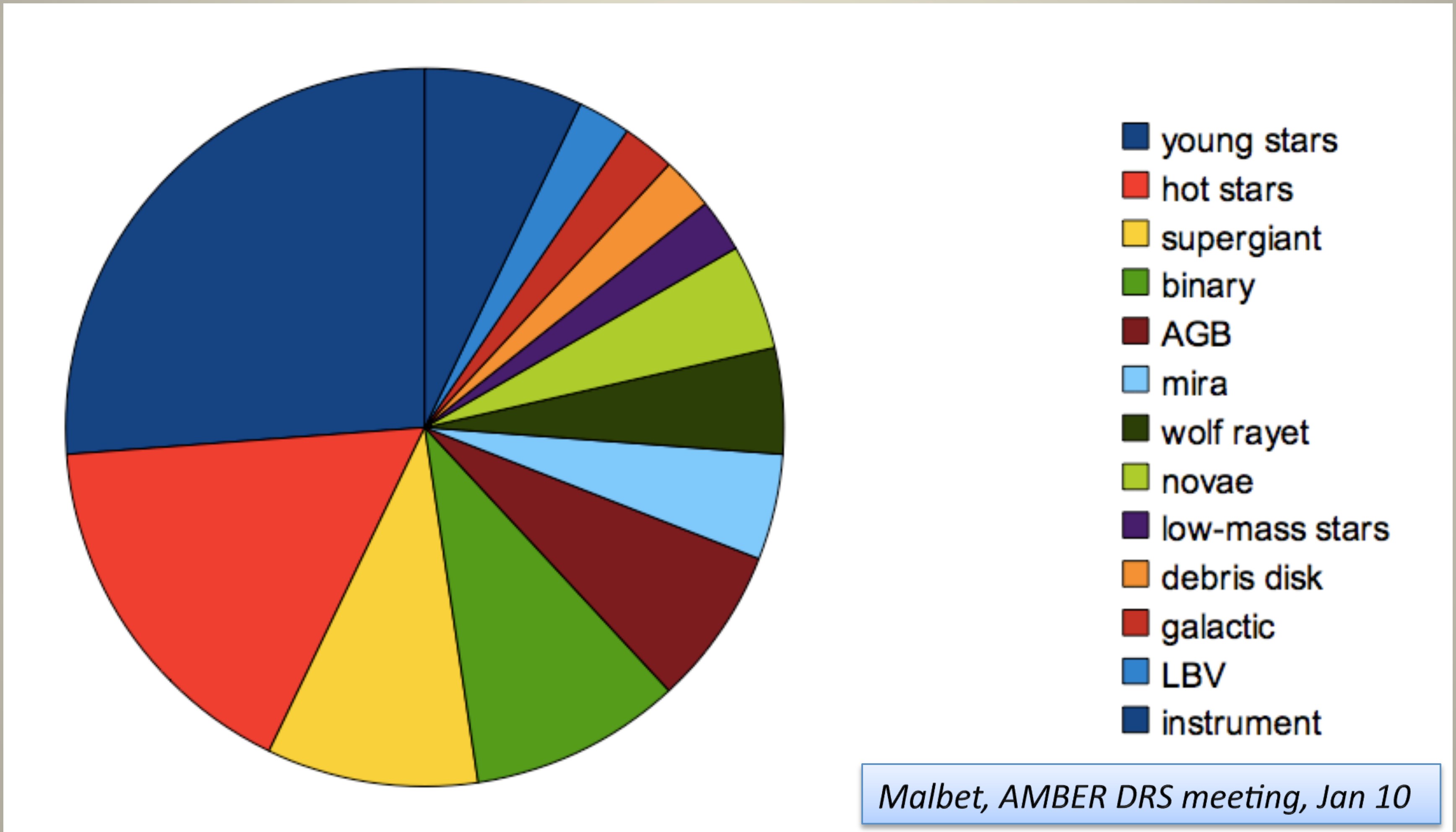

Malbet, AMBER DRS meeting, Jan 10

AMBER Science topics

(Accepted refereed publications, January 2014)

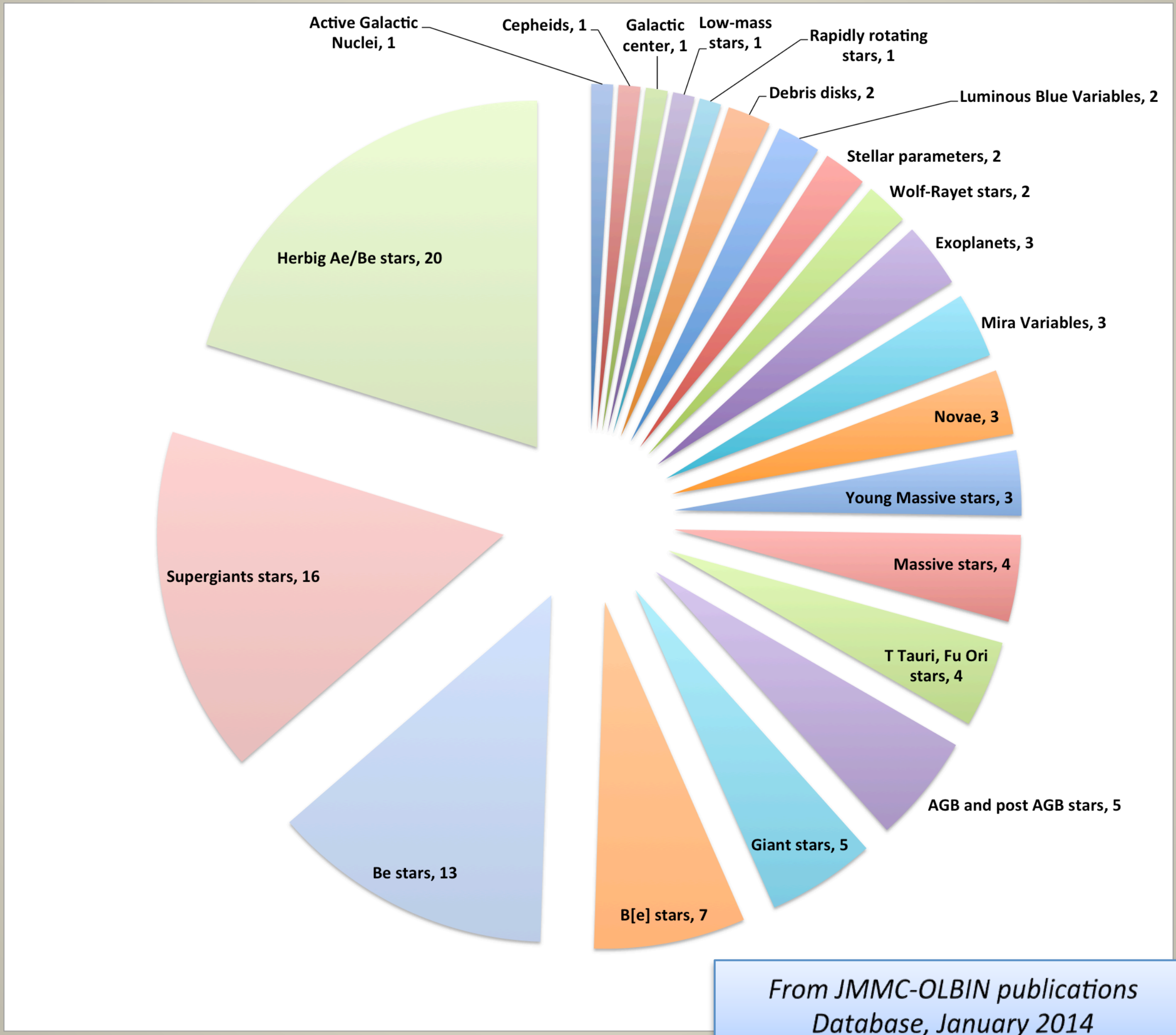

From JMMC-OLBIN publications Database, January 2014